Numerical investigation of high-temperature effects in the UTIAS–RPI hypersonic impulse tunnel

C. P. T. Groth, J. J. Gottlieb, and P. A. Sullivan

Institute for Aerospace Studies, University of Toronto, 4925 Dufferin Street, Downsview, Ont., Canada M3H 5T6

The hypersonic impulse tunnel of the University of Toronto Institute for Aerospace Studies (UTIAS) and Ryerson Polytechnical Institute (RPI) is a short-duration blow-down experimental wind tunnel capable of producing high-Mach-number flows ($Ma \approx 8$). A generalized quasi-one-dimensional nonstationary flow analysis and associated total-variation-diminishing (TVD) finite-difference solution schemes, including aproximate Riemann solvers, are presented for predicting the high-temperature flows in such facilities. The analysis is used to investigate the operation of the UTIAS–RPI facility and produce performance data that are not always easily determined or available from experimental measurements. The thermodynamic state of the nozzle-exit flow and high-temperature or real-gas effects are assessed for this facility under various operating conditions. Numerical results, coupled with additional comparisons with available experimental data, demonstrate the range of test-section flows that may be achieved. They also illustrate that for typical operating conditions, the air (working gas used in UTIAS–RPI facility) *freezes* in the nozzle very close to the throat and results in test-section flows with considerable energy bound in the vibrational modes of the nitrogen (N_2) and oxygen (O_2) molecules. In particular, the test-section temperatures associated with the vibrational modes of N_2 are only marginally less than barrel-end stagnation temperatures, whereas the vibrational temperatures of O_2, although lower than stagnation temperatures, are still much higher than the predicted translational–rotational temperatures.

Le tunnel hypersonique à impulsions de l'Institut d'études aérospatiales de l'Université de Toronto (UTIAS) et de l'Institut polytechnique Ryerson (RPI) est une soufflerie expérimentale à rafales de courte durée, capable de produire des écoulements à nombre de Mach élevé ($Ma \approx 8$). On présente une analyse généralisée d'écoulement non stationnaire quasi unidimensionnel, ainsi que des méthodes de solution par différences finies avec diminution de la valeur totale, incluant des résolveurs de Rieman approximatifs, afin de faire des prédictions pour les écoulements à haute température dans de telles installations. On utilise cette analyse pour étudier le fonctionnement de la soufflerie UTIAS–RPI et récueillir des données sur sa performance, laquelle n'est pas toujours facile à déterminer ou disponible à partir de mesures expérimentales. L'état thermodynamique de l'écoulement à la sortie de la tuyère et les effets de haute température ou de gaz réel sont établis pour différentes conditions de fonctionnement de l'installation. Les résultats numériques, couplés à des comparaisons additionnelles avec les données expérimentales disponibles, indiquent quelle est la gamme d'écoulement qu'on peut obtenir pour les essais. Ils montrent aussi que dans des conditions typiques de fonctionnement, l'air (gaz utilisé dans la soufflerie UTIAS–RDI) *gèle* dans la tuyère, près de la partie la plus étroite, ce qui donne dans la section des tests des écoulements avec une énergie considérable liée aux modes vibrationnels des molécules d'azote (N_2) et d'oxygène (O_2). En particulier, les températures de la section des tests associées aux modes vibrationnels de N_2 ne sont que marginalement inférieures aux températures de stagnation à l'extrémité du tunnel, alors que les températures vibrationnelles de O_2, bien qu'elles soient inférieures aux températures de stagnation, sont encore beaucoup plus élevées que les températures de translation–rotation prédites.

[Traduit par la rédaction]

1. Introduction

Recently, there has been a renewed interest in hypersonic aerodynamics. The increased research activity in this area was stimulated primarily by a number of major initiatives such as the National Aerospace Plane (NASP) and Aeroassisted Orbital Transfer Vehicle (AOTV) projects in the United States, as well as the European Hermes project. The concept of a viable transatmospheric vehicle for commercial use has also added to this interest.

The physics of hypersonic flow is significantly different from that of the subsonic, transonic, and supersonic flow regimes. Very high temperatures are one characteristic of the hypersonic flow environment. The presence of strong normal shock waves in the stagnation regions of hypersonic flows and the extreme viscous dissipation that occurs within hypersonic boundary layers can create very high temperatures. For example, atmospheric re-entry temperatures can reach 11 000 K. Such temperatures are severe enough to excite vibrational energy modes, cause dissociation, and even ionize the air molecules. For air, vibrational excitation typically becomes important at temperatures above 800 K, dissociation of oxygen molecules begins at about 2000 K, and ionization becomes significant once tem-

peratures exceed 8000 K (1–3). The occurrence of any or all of these so-called *high-temperature* or *real-gas* effects brings about a dramatic departure in the thermodynamic behaviour of the gas from that of the ideal. They must be considered in the design of any advanced hypersonic transportation system, if the problems of surface heating and aerodynamic loading are to be properly addressed.

Flow-scaling or similitude arguments dictate that the vehicle scale must be duplicated as well as the velocity and altitude, in any simulation of hypersonic flow undergoing nonequilibrium chemistry (4, 5). This is not possible in existing ground-based experimental facilities and full-scale flight tests are required in many cases. Consequently, computational fluid dynamics (CFD) has become a particularly important design tool in hypersonic aerodynamics, much more so than for conventional aircraft design. However, experimental hypersonic research programs are still necessary to provide a reliable experimental data base encompassing a variety of flow conditions for validation of the CFD computer codes. Furthermore, practical design information can often be obtained by combining experimental results from several different test facilities.

The so-called *impulse, gun,* and (or) *free-piston shock tunnels* (4, 6–9) are representative of a class of experimental facil-
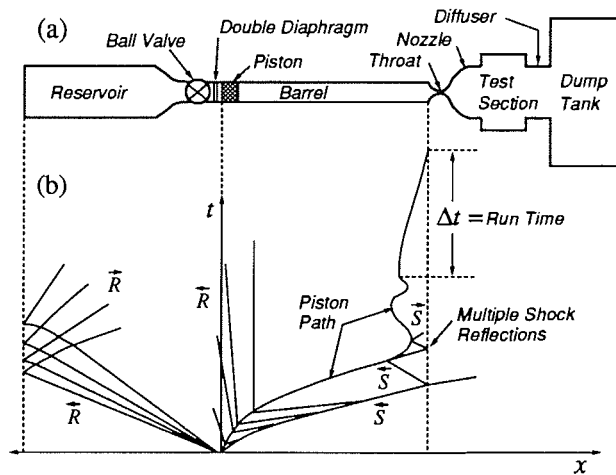
FIG. 1. UTIAS hypersonic impulse tunnel. (a) Schematic diagram of facility, (b) x–t diagram of tunnel operation.

ities that have been used successfully to simulate various aspects of hypersonic flight in the laboratory (primarily Mach number and to some extent Reynolds number). A facility of this sort has been recently refurbished and brought into operation by the University of Toronto Institute for Aerospace Studies (UTIAS) and Ryerson Polytechnical Institute (RPI) (10). In this impulse tunnel, a high-pressure driver gas is used to accelerate a piston. This accelerating piston compresses and heats the working gas (air) by means of a multiple-shock nonisentropic process for subsequent expansion through a contoured nozzle to a high Mach number. The use of the piston to separate the driver and working gases is what differentiates the impulse tunnel from *shock tunnels* (4, 9, 11–13), another related class of hypersonic test facility. Note that impulse tunnels offer several advantages. They generally have relatively longer run times than alternate intermittent devices such as shock tunnels and are considerably less costly than continuous or steady-state operating facilities.

The determination of stagnation pressure, stagnation enthalpy or total temperature (a useful measure of the thermodynamic state of the test-section flow), thermodynamic processes in the nozzle of the impulse tunel, and test-section flow properties are all required for accurate interpretation of experimental data; however, many of these facility characteristics are difficult to measure directly. Furthermore, a thorough understanding of the tunnel operation is required to explore various avenues for extending the range of flow conditions that may be simulated. Previous studies have generally employed simplified analytic techniques to investigate various aspects of tunnel performance (see, for example, refs. 14–20). More recently, a simplified quasi-one-dimensional numerical model has been proposed for the starting process in the nozzle of a free-piston shock tunnel (21). This paper presents a fairly sophisticated quasi-one-dimensional nonstationary compressible flow analysis and related numerical solution algorithm that have been developed for predicting the complete unsteady performance and operation of the UTIAS-RPI hypersonic impulse tunnel. The analysis is capable of predicting barrel stagnation and test-section flow properties, unsteady piston motion, run times, as well as the high-temperature effects associated with the impulse tunnel flows. Modeling and algorithm details, comparisons with experimental data, and predictions of tunnel performance are all described.

2. Description of impulse tunnel

The UTIAS–RPI hypersonic impulse tunnel is a blow-down or short-duration test facility in which the high stagnation temperatures for the nozzle flows are generated by a shock compression process. A schematic of the experimental facility is depicted in Fig. 1a. The tunnel consists of a 5.6 m long reservoir or driver with an internal radius of 152.4 mm and a 6.4 m long barrel with an internal radius of 38.1 mm that are separated by an isolating ball valve and a double diaphragm. A relatively light aluminum piston weighing approximately 95 g is free to move in the barrel. Various convergent–divergent nozzles may be connected to the barrel at the nozzle breech. A 1.54 m long nozzle with throat and exit radii of 6.35 and 108.87 mm, respectively, is currently employed. This nozzle has a design Mach number of 8.33. The nozzle projects into a 0.61 m long test section with a rectangular cross section of 0.61 × 0.64 m², which is in turn connected by a diffuser to a relatively large dump tank with a volume of approximately 2.85 m³. The initial pressure of the driver gas (currently air) in the reservoir is normally maintained at 20.5 MPa and initial barrel pressure for the working gas (again this is usually air) ranges between 200 and 800 kPa. A small Lexan plug is placed in the throat of the nozzle so that the test section can be evacuated down to pressures nearing 50 Pa.

During tunnel operation, the double diaphragm is burst and the high-pressure driver gas rapidly accelerates the piston along the barrel. The accelerating piston creates a series of multiple shock reflections in the barrel that heat and compress the working gas. The nozzle throat plug is expelled by the first reflected shock and the working gas then flows through the convergent–divergent nozzle and on through the test section. The piston eventually comes to rest at the end of the barrel when the working gas is depleted. Typical run times for this facility are between 10–30 ms. The impulse tunnel operation is illustrated in the x–t wave diagram of Fig. 1b. The primary shock and rarefaction wave patterns characterizing the nonstationary wave interaction processes occurring in the tunnel, indicated by S and R, respectively, are shown in this figure. Note that a more complete description of the UTIAS–RPI hypersonic impulse tunnel, which includes details of tunnel instrumentation and calibration, may be found in ref. 10.

3. Equations of motion

The complex unsteady flow of the driver and working gases in the reservoir, barrel, and nozzle behind and in front of the accelerating piston are modeled by solving the equations of motion (continuity, momentum, and energy) for generalized one-dimensional nonstationary compressible flows in ducts. The equations include inhomogeneous source terms associated with the flow driving potentials of area change, friction, heat transfer, and head loss and are well documented in many textbooks (see, for example, ref. 22). They have been used successfully in previous studies to predict nonstationary flows in other experimental facilities such as blast-wave simulators and two-stage light-gas hypervelocity launchers (23–25). The weakly conservative forms of these partial differential equations may be expressed as

$$[1] \quad \frac{\partial}{\partial t}(U) + \frac{\partial}{\partial x}[F(U)] = A(U) + S(U)$$

where the multicomponent solution and flux column vectors U and F are given by

$$[2] \quad U = \begin{bmatrix} \rho \\ \rho u \\ \rho\left(e + \dfrac{u^2}{2}\right) \end{bmatrix}, \quad F = \begin{bmatrix} \rho u \\ \rho u^2 + p \\ \rho u\left(e + \dfrac{p}{\rho} + \dfrac{u^2}{2}\right) \end{bmatrix}$$

the source flux column vectors A and S are defined by

$$[3] \quad A = \begin{bmatrix} -\rho u \dfrac{1}{A}\dfrac{dA}{dx} \\[2ex] -\rho u^2 \dfrac{1}{A}\dfrac{dA}{dx} \\[2ex] -\rho u\left(e + \dfrac{p}{\rho} + \dfrac{u^2}{2}\right)\dfrac{1}{A}\dfrac{dA}{dx} \end{bmatrix}, \quad S = \begin{bmatrix} 0 \\ F_{wall} + F_{loss} \\ Q_{wall} + Q_{zero} \end{bmatrix}$$

and the symbols ρ, u, p, and e denote the gas density, velocity, pressure, and total specific internal energy, and x and t are position and time. The variable A is the local cross-sectional area of the duct, which is taken to be a known function of x. The other terms appearing in column vectors A and S represent the effects of area change, boundary-layer friction, wall heat transfer, and other flow pressure or head losses. F_{wall} is an equivalent body force per unit volume to account for viscous or frictional losses in the boundary layer near the wall of the duct flow. F_{loss} is a similar body force per unit volume that includes additional pressure losses for flows through area changes and over diaphragm remnants. The variable Q_{wall} denotes the heat transfer rate per unit volume from the duct walls to the gas and the variable Q_{zero} represents the time rate of change in the zero-point energy of the gas resulting from chemical reactions. This latter term is required when modeling finite-rate reaction processes.

The body force due to boundary layer friction can be expressed in the form

$$[4] \quad F_{wall} = -\frac{f}{D_h}\frac{\rho u|u|}{2}$$

where f is the Darcy–Weisbach friction factor and D_h is the local hydraulic diameter of the duct ($D_h = 2\pi r$ for pipes where r is the radius). In this study, the friction factor is obtained by using

$$[5] \quad f = \begin{cases} \dfrac{64}{Re\Lambda}, & 0 < Re < 2000 \\[2ex] \dfrac{0.032}{\Lambda}\left[\dfrac{Re}{2000}\right]^{0.3187}, & 2000 \leq Re \leq 4000 \\[2ex] \left[1.14 - 2\log_{10}\left(21.25Re^{-0.9} + \dfrac{\epsilon}{D_h}\right)\right]^{-2}\Lambda^{-1}, & Re > 4000 \end{cases}$$

for which $Re = \rho|u|D_h/\mu$ is the local Reynolds number, μ is the gas viscosity, and ϵ denotes the absolute roughness of the wall surface. The previous relationships are taken from steady pipe flow theory. The first expression is the well-known theoretical result from Hagen–Poiseuille flow, which describes the friction factor in the laminar regime ($0 < Re < 2000$), the third is an explicit empirical expression developed by Jain (26) valid in the fully turbulent regime ($Re > 4000$), and the other expression provides estimates for the friction factor in the transitional regime ($2000 \leq Re \leq 4000$). Note that Λ is a compressibility correction factor. It is calculated from the semi-empirical relation

$$\Lambda = 1 + \frac{(\gamma - 1)\Omega(Ma)^2}{2}$$

as suggested by Liepmann and Goddard (27), where γ is the specific heat ratio of the gas, Ma is the local flow Mach number, and Ω is the recovery factor. This last parameter can be approximated by $(Pr)^{1/2}$ for laminar flows and $(Pr)^{1/3}$ for turbulent flows where Pr is the Prandtl number for the gas.

Similarly, the body forces due to pressure or head losses in the flow can be written as

$$[6] \quad F_{loss} = -\frac{K}{L}\frac{\rho u|u|}{2}$$

where K is the head-loss coefficient and L is the finite duct length over which the losses are distributed ($L = 2D_h$ in this study). Although these losses are usually small, values for K can range between 0–10 depending on the flow obstructions.

The rate of heat transfer to the gas from the wall per unit volume of the flow Q_{wall} is prescribed by employing the semi-empirical form of Reynolds' analogy for compressible pipe flow suggested by Colburn (28). The heat transfer rate is thus given by

$$[7] \quad Q_{wall} = \frac{4k\,Nu}{D_h^2}[T_w - T_{aw}]$$

$$= \frac{fC_p\rho|u|}{2(Pr)^{2/3}D_h}[T_w - \Lambda T]$$

where Nu, k, and C_p, T, and T_{aw} are the gas Nusselt number, thermal conductivity, specific heat at constant pressure, temperature, and adiabatic wall temperature, respectively, and T_w is the local duct wall temperature. Note that the Prandtl number is defined by

$$Pr = \frac{\mu C_p}{k}$$

and the effects of compressibility appear in [7] via the friction factor f and correction factor Λ.

The piston of the UTIAS–RPI hypersonic impulse tunnel is basically a thick aluminum disc with a trailing tapered skirt that provides stability during motion. Holes are machined through the skirt to reduce weight. To model the piston motion in the barrel, it is assumed that the piston is a rigid cylinder of length L_p and radius r_p. Newton's law is then applied with pressure, inertial, and viscous-drag forces all taken into account. This results in a differential equation for the piston motion, which can be written as

$$[8] \quad m_p\frac{dV_p}{dt} = \pi r_p^2(p_f - p_b) + F_p$$

where V_p is the piston velocity, p_f and p_b are the front and back face pressures exerted on the piston by the high-pressure gases, F_p is the frictional force acting on the piston, and m_p is the piston mass. The friction force is determined by assuming that a quasi-steady Couette flow exists between the exterior surface of the piston and the tunnel walls and a Reynolds number correlation similar to those for fully developed pipe flow is used to determine the frictional shear stress at the piston surface. F_p can then be approximated by

$$[9] \quad F_p = -2\pi r_p L_p(1 - \sigma)f_p\left[\frac{\mu V_p}{r - r_p}\right]$$

where f_p is the piston friction factor having the form

$$f_p = cRe_p^n$$

and

$$Re_p = \frac{\rho V_p(r - r_p)}{\mu}$$

is the piston Reynolds number; c and n are constants. The variable σ ($0 \leq \sigma < 1$) is the porosity of the piston skirt.

4. Thermodynamic models for air

At the present time, air is used almost exclusively as the driver and working gas in the UTIAS–RPI hypersonic impulse tunnel. Thermodynamic and caloric models are required to

interrelate the various intensive properties of air, such as pressure, temperature, and internal energy, and thereby complete or close the governing set of equations given by [1]–[7]. In this study, three different models are employed to describe the thermodynamic and transport properties of air. They are the perfect-gas model (polytropic or thermally and calorically perfect gas), an equilibrium real-gas model, and a nonequilibrium (vibrationally relaxing and chemically reacting) high-temperature model. The three different thermodynamic models are very helpful in assessing the magnitude of the high-temperature effects in the impulse tunnel flows and the departure of the working gas behaviour from the ideal.

4.1. Polytropic model

For polytropic gases, the pressure and temperature can be related to the density and total specific internal energy using the well-known ideal-gas equation of state

$$[10] \quad p = \rho RT = (\gamma - 1)\rho e$$

where γ is the specific heat ratio, R is the gas constant, and

$$C_p = \frac{\gamma R}{\gamma - 1}$$

In the case of air, the values of γ and R are taken to be 1.40 and 287.06 Pa m^3 (kg K)$^{-1}$, respectively. The sound speed a can also be related to the other intensive properties by the expressions

$$[11] \quad a^2 = \gamma RT = \gamma\frac{p}{\rho} = \gamma(\gamma - 1)e$$

The polytropic model is completed by employing semi-empirical expressions for the dynamic viscosity and Prandtl number. An empirical extension of Sutherland's law of the form

$$[12] \quad \mu = \frac{c_1 T^{3/2}}{c_2 + T^{c_3} + \dfrac{c_4}{T}}$$

is used, where c_1, c_2, c_3, and c_4 are constants and equal to 5.2192×10^{-7}, -3.31132, 0.865351, and 2365.27, respectively, for air. The Prandtl number for air depends primarily on the specific heat ratio. A modified form of Euken's formula is used herein to prescribe the Prandtl number. The formula is based on some ideas of Chapman and Cowling (29) and given by

$$[13] \quad Pr = \frac{20\gamma}{39\gamma - 15}$$

which is in good agreement with experimental data.

4.2. Equilibrium model

The curve fits of Srinivasan, et al. (30) and Srinivasan and Tannehill (31) are used to represent the equilibrium thermodynamic and transport properties of air. These curve fits are constructed from bicubic polynomials and Grabau-type transition functions to model the thermodynamic properties in a piecewise manner. They are valid for temperatures up to 25 000 K. The correlations for the pressure p, temperature T, sound speed a, viscosity μ, Prandtl number Pr, and thermal conductivity $k = \mu C_p/Pr$ in the form

$$p = p(\rho, e), \qquad T = T(\rho, e), \qquad a = a(\rho, e)$$

$$\mu = \mu(\rho, T), \qquad Pr = Pr(\rho, T), \qquad k = k(\rho, e)$$

are all employed. Note that if the equation of state has the form

$$p = p(\rho, e)$$

then the sound speed can be related to the pressure, density, and internal energy by the relationship

$$[14] \quad a^2 = \left.\frac{\partial p}{\partial \rho}\right|_s = \left.\frac{\partial p}{\partial \rho}\right|_e + \frac{p}{\rho^2}\left.\frac{\partial p}{\partial e}\right|_\rho$$

where s is the entropy.

4.3. Nonequilibrium model

The thermodynamics of the nonequilibrium air is modeled by treating it as a chemically reactive mixture of thermally perfect gases for which the thermal state can be described by the following separate and independent temperatures (or internal energies): a translational–rotational temperature and the vibrational temperatures of the polyatomic species. The translational–rotational temperature represents the contribution to the internal energy by the translational and rotational modes of all molecules and atoms in the mixture. These modes are assumed to be in equilibrium, which is a reasonable approximation for most continuum flow studies (1). Each vibrational temperature represents the contribution to the internal energy by the vibrational modes of the corresponding polyatomic species. Intermolecular forces, electronic excitation, and ionization effects are all neglected.

Additional equations for species mass and vibrational energy are necessary for describing the one-dimensional flow of a nonequilibrium mixture. They may be written as (32)

$$[15] \quad \frac{\partial W}{\partial t} + u\frac{\partial W}{\partial x} = Q(W)$$

where the column vectors W and Q are defined by

$$W = \begin{bmatrix} c_1 \\ \vdots \\ c_N \\ c_1 e_{v_1} \\ \vdots \\ c_N e_{v_N} \end{bmatrix}$$

$$[16]$$

$$Q = \begin{bmatrix} w_1 \\ \vdots \\ w_N \\ c_1 q_1 + \beta_1 w_1 e_{v_1} \\ \vdots \\ c_N q_N + \beta_N w_N e_{v_N} \end{bmatrix}$$

and where $c_s = \rho_s/\rho$ is the mass fraction of species s with $\Sigma_s c_s = 1$, ρ_s is the density of species s, e_{v_s} is the specific vibrational energy of species s, $e_v = \Sigma_s c_s e_{v_s}$ is the total specific vibrational energy of the mixture, and N is total number of species in the

mixture. The variable w_s represents the time rate of change of the concentration of the species s brought about by the chemical reactions. The variable q_s represents the time rate of change of the vibrational energy of the species s brought about by relaxation to its equilibrium value. Finally, the term $\beta_s w_s e_{v_s}$ appearing in [15] and [16] is related to the change in the vibrational energy of species s per unit volume of the mixture due to the chemical reactions. The quantity β_s is an empirical value greater than or equal to unity. It is introduced to reflect the observed preference of *higher than average* vibrationally excited molecules to dissociate and the tendency of atoms to combine and form higher than average vibrationally excited molecules (32).

The total specific internal energy of the thermally perfect gaseous mixture is the sum of translational–rotational and vibrational energies and given by

$$[17] \quad e = e_{tr} + e_v = e_{tr} + \sum_{s=1}^{N} c_s e_{v_s}$$

where e_{tr} is the translational–rotational energy. The mixture pressure may then be expressed in terms of the translational–rotational temperature T and (or) energy e_{tr} and the various mixture properties by employing the ideal equation of state for each thermally perfect species and applying Dalton's law of partial pressure. The resulting equation of state for the mixture is

$$[18] \quad p = \rho RT = (\gamma - 1)\rho e_{tr}$$

where

$$R = \mathcal{R} \sum_s \frac{c_s}{\mathcal{M}_s} = \sum_s c_s R_s$$

is the specific gas constant of the mixture, $\mathcal{R}$ is the universal gas constant, $\mathcal{M}_s$ is the molecular weight of species, s, $R_s = \mathcal{R}/\mathcal{M}_s$ is the specific gas constant of species s, and
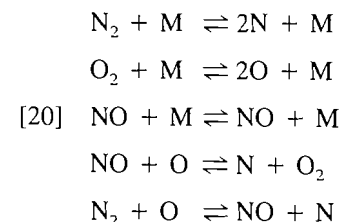
$$\gamma = 1 + \frac{\sum_s c_s R_s}{\sum_s \frac{c_s R_s}{(\gamma_s - 1)}}$$

is defined to be the *frozen* specific heat ratio of the mixture. The variable γ_s represents the frozen specific heat ratio of species s (i.e., the specific heat ratio species in the absence vibrational excitation). It is also possible to define a frozen sound speed for the mixture. This intensive property may be related to the other mixture properties by the expression

$$[19] \quad a^2 = \gamma RT = \gamma\frac{p}{\rho} = \gamma(\gamma - 1)e_{tr}$$

where a is the frozen sound speed.

In this work, a five-species (N_2, O_2, NO, N, and O) four-temperature (i.e., translational–rotational temperature T, and vibrational temperatures T_{vN_2}, T_{vO_2}, and T_{vNO}) nonequilibrium thermodynamic model of air is employed. The model is valid for temperatures up to 8000 K and pressures above 1 kPa. In his model, the dissociation–recombination reaction mechanism of air is represented by the elementary reactions

$$N_2 + M \rightleftharpoons 2N + M$$

$$O_2 + M \rightleftharpoons 2O + M$$

$$[20] \quad NO + M \rightleftharpoons NO + M$$

$$NO + O \rightleftharpoons N + O_2$$

$$N_2 + O \rightleftharpoons NO + N$$

where M is a collision partner; it can be any of the five species. Collision theory is used to describe the finite-rate reaction processes from which empirical expressions for the time rate of change of the species concentrations may be obtained. These expressions have the form (1–3)

$$[21] \quad w_s = \mathcal{M}_s \sum_{r=1}^{N_R} (\sigma_{s,r}^b - \sigma_{s,r}^f) \left\{ k_r^f \prod_{s'=1}^{N} \left(\frac{c_{s'}}{\mathcal{M}_{s'}} \right)^{\sigma_{s',r}^f} - k_r^b \prod_{s'=1}^{N} \left(\frac{c_{s'}}{\mathcal{M}_{s'}} \right)^{\sigma_{s',r}^b} \right\}$$

where $\sigma_{s,r}^f$ and $\sigma_{s,r}^b$ are the stoichiometric coefficients of the reactant and product species s for the reaction r, and k_r^f and k_r^b are the forward and backward reaction rates of reaction r. The variable N_R represents the total number of elementary reactions. The reaction rates are assumed to be functions of the rotational–translational temperature and are described by modified forms of the Arrhenius equation. They are given by

$$[22] \quad k_r^f = C_r^f T^{n_r^f} \exp\left(\frac{-E_r^f}{KT} \right), \qquad k_r^b = C_r^b T^{n_r^b} \exp\left(\frac{-E_r^b}{KT} \right)$$

The reaction rate coefficients C_r^f, C_r^b, n_r^f, n_r^b, E_r^f, and E_r^b of [22] are taken from the data set compiled by Dunn and Kang (33).

The finite-rate vibrational relaxation of the diatomic molecules is represented in the five-species four-temperature nonequilibrium model of air by assuming that the vibrationally excited molecules behave as ideal harmonic oscillators. It is further assumed that the relaxation process from an excited nonequilibrium state to a state of thermodynamic equilibrium (i.e., $T = T_{vN_2} = T_{vO_2} = T_{vNO}$) occurs only through translational–vibrational collisions. Under these assumptions, it is possible to prescribe the time rate of change of the vibrational energy of the species s by (1–3)

$$[23] \quad q_s = \frac{e_{v_s}^* - e_{v_s}}{\tau_s}$$

where e_v^* is the local equilibrium temperature given by

$$[24] \quad e_{v_s}^* = \frac{\Theta_{v_s} R_s}{\exp\left(\dfrac{\Theta_{v_s}}{T} \right) - 1}$$

and τ_s is the characteristic relaxation time. The characteristic vibrational temperatures Θ_{vN_2}, Θ_{vO_2}, and Θ_{vNO} are taken to be 3353, 2239, and 2699 K, respectively. The semi-empirical correlations of Millikan and White (34) based on modifications to the Landau–Teller equation are used to determine τ_s. These correlations have the form

$$[25] \quad \tau_s = \frac{\displaystyle\sum_{s'} \frac{c_{s'}}{\mathcal{M}_{s'}} \exp\left\{ \mathcal{A}_s \left[T^{-1/3} - 0.015 \left(\frac{\mathcal{M}_s \mathcal{M}_{s'}}{\mathcal{M}_s + \mathcal{M}_{s'}} \right)^{1/4} \right] - 18.42 \right\}}{p \displaystyle\sum_{s'} \frac{c_{s'}}{\mathcal{M}_{s'}}}$$

and $\mathcal{A}_{N_2}$, $\mathcal{A}_{O_2}$, and $\mathcal{A}_{NO}$ are assumed to have values of 220, 129, and 168, respectively.

Using the preceding relations, it is possible to prescribe the source term Q_{zero} of [1] that represents the total change in the zero-point energy of the mixture resulting from the chemical reactions by the expression

$$[26] \quad Q_{zero} = -\rho \sum_{s=1}^{N} w_s \Delta h_{f_s}^0$$

where $\Delta h_{f_s}^0$ is the heat of formation of species s evaluated at a temperature of 0 K. The heats of formation for the five species were taken to be $\Delta h_{fN_2}^0 = 0$, $\Delta h_{fO_2}^0 = 0$, $\Delta h_{fNO}^0 = 2991.89$ kJ kg^{-1}, $\Delta h_{fN}^0 = 33\,613.91$ kJ kg^{-1}, and $\Delta h_{fO}^0 = 15\,424.95$ kJ kg^{-1}. Note that Q_{zero} is identically zero for the polytropic and equilibrium models. Note additionally that the effect of the preferential dissociation of vibrationally excited diatomic molecules is not included herein and β_s is taken to be unity in this work.

Finally, transport properties of nonequilibrum air required for the determination of the boundary-layer friction F_{wall} and heat transfer Q_{wall} in [1]–[3] are computed as follows. The mixture specific heat and Prandtl number are approximated by the frozen flow (i.e., polytropic-gas equivalent) relations

$$C_p = \frac{\gamma R}{(\gamma - 1)}$$

and

$$Pr = \frac{20\gamma}{(39\gamma - 15)}$$

respectively. The viscosity of each species μ_s is defined in terms of the translational–rotational temperature T by using the semi-empirical correlations of Blottner *et al.* (35) given by

[27] $\mu_s = 0.10 \exp [(b_{1_s} \ln T + b_{2_s}) \ln T + b_{3_s}]$

and the mixture or total viscosity is calculated by employing the semi-empirical mixing rule of Wilke (36) as follows:

[28] $\displaystyle \mu = \sum_{s=1}^{N} \frac{c_s \mu_s}{\mathcal{M}_s \phi_s}$

where

[29] $\displaystyle \phi_s = \sum_{s'=1}^{N} \frac{c_{s'}}{\mathcal{M}_{s'}} \left[1 + \left(\frac{\mu_s}{\mu_{s'}} \right)^{1/2} \left(\frac{\mathcal{M}_{s'}}{\mathcal{M}_s} \right)^{1/4} \right]^2 \left[8 \left(1 + \frac{\mathcal{M}_s}{\mathcal{M}_{s'}} \right) \right]^{-1/2}$

The curve fits of [27] are appropriate for temperatures up to 10 000 K and the constant coefficients b_{1_s}, b_{2_s}, and b_{3_s} for each species are taken from ref. 35.

5. Numerical solution procedure

General solutions to the preceding equations prescribing the flow of the impulse tunnel driver and working gases and the motion of the piston in the barrel and must be obtained numerically. The differential equation for the piston motion given by [8] can be integrated by decoupling it from the gas dynamic equations and employing the most recent flow field solution in a forward Euler time-stepping procedure. This simple approach is sufficiently accurate and robust as the characteristic time scales associated with the piston motion are very much larger than the gas dynamic time scales. The gas dynamic equations given by [1]–[3] may then be solved in a separate integration procedure where, at each level or time step, the corresponding updated solution for the piston motion is employed. However, the numerical solution of this inhomogeneous system of hyperbolic conservation laws is made difficult by the presence of large solution gradients and strong shocks. It is further complicated if source terms are stiff. Classical first-order shock-capturing finite-difference schemes can require excessive grid refinement to resolve the complicated shock structure, and second-order schemes can lead to spurious Gibb's oscillations or nonlinear instabilities near discontinuities. In the last 5–10 years, solution-dependent nonlinear higher order methods have been developed, such as the total-variation-diminishing (TVD) finite-difference schemes of Harten (37, 38), Roe (39–41), Davis (42), Yee (43), and Chakravarthy and Osher (44, 45). They are very appropriate for the hyperbolic system considered here. These schemes effectively eliminate oscillations near extrema, limit numerical diffusion, maintain higher order accuracy wherever possible, and thereby permit the efficient resolution of weak solutions.

In this study, the explicit higher order TVD upwind difference scheme of Roe (39, 40, 46) is used to solve the governing partial differential equations of the gaseous flows when supplemented by the ancillary equations of the polytropic and equilibrium thermodynamic models. Roe's approximate Riemann solver is used in the evaluation of the numerical fluxes for the polytropic case and an extension of this approximate solver proposed by Glaister (47) is employed for the equilibrium case.

When supplemented with nonequilibrium thermodynamic model equations, the solution of [1] is complicated by the additional species mass and vibrational energy conservation equations [15], as well as the presence of inhomogeneous source terms representing the finite-rate vibrational relaxation and chemical reaction processes. The additional source terms are often large and can make the solution algorithms stiff (i.e., the time-stepping of a marching procedure is drastically constrained by stability considerations rather than by the usual accuracy concerns). In this case, the gas dynamic and thermodynamic equation sets are partially decoupled by employing a *frozen flow* approximation. Both sets of decoupled equations are then integrated alternately in a lagged manner within a time-marching procedure. A semi-implicit version of the Roe's scheme is applied to each equation set. The inhomogeneous source terms associated with the finite-rate processes are treated implicitly in the time-stepping scheme and an extension of Roe's approximate Riemann solver is used to evaluate the numerical flux functions. The extended Riemann solver provides the eigenvalues and eigenvectors of the fully coupled system.

Further details of these TVD shock-capturing schemes are given in the following subsections. The various algorithm extensions particular to this application are discussed. This includes the approximate Riemann solvers, partial-decoupling procedure, implicit treatment of stiff source terms, and boundary conditions.

5.1. Solution algorithm for polytropic and equilibrium gas flows

TVD schemes were originally developed for solving linear and nonlinear scalar homogeneous hyperbolic conservation laws in one space dimension. Algorithm extensions are necessary to deal with the vector nature and source terms of inhomogeneous systems of differential equations. In Roe's flux-differencing method, a local characteristic approach is adopted in which the properties of the inviscid flux Jacobians are utilized in conjunction with approximate Riemann solvers to represent the solution and flux vector jumps in terms of characteristic variables. A TVD algorithm is then applied to each characteristic field in a *scalar* fashion. Source terms may be treated either explicitly or implicitly depending on the nature of the equations.

In the case of the polytropic and equilibrium thermodynamic models, Roe-method solutions of the one-dimensional three-component system given by [1] can be formulated as follows. Let U_i^n be the numerical approximation of the solution at discrete locations $x = x_i$ and time $t = t^n$. The solution at subsequent time levels is obtained by means of the time-stepping procedure

[30] $U_i^{n+1} = \mathscr{L}_U^{\Delta t} U_i^n$

where the solution operation $\mathcal{L}_U^{\Delta t}$ advances the solution U through a time interval $\Delta t''$ with

$$\Delta t'' = t''^{+1} - t''$$

and is defined by the two-stage difference scheme

[31] $\quad U_i^{\overline{n+1}} = U_i^n + \Delta U_i^{\overline{n}}$

$$= U_i^n + \Delta t''(A_i^n + S_i^n) - \frac{1}{2} \sum_{k=1}^{3} \{[(v_{i+1/2,k}^n - |v_{i+1/2,k}^n|) + \phi_{i+1/2,k}^n |v_{i+1/2,k}^n| (1 - |v_{i+1/2,k}^n|)]\Delta U_{i+1/2,k}^n$$

$$+ [(v_{i-1/2,k}^n + |v_{i-1/2,k}^n|) - \phi_{i-1/2,k}^n |v_{i-1/2,k}^n| (1 - |v_{i-1/2,k}^n|)]\Delta U_{i-1/2,k}^n\}$$

[32] $\quad U_i^{n+1} = U_i^n + \Delta U_i^n = U_i^{\overline{n+1}} + \frac{1}{2}\Delta t'' (A_i^{\overline{n+1}} - A_i^n + S_i^{\overline{n+1}} - S_i^n)$

and where

$$\Delta U_i^n = U_i^{\overline{n+1}} - U_i^n, \Delta U_i^{\overline{n}} = U_i^{\overline{n+1}} - U_i^n$$

and $U_i^{\overline{n+1}}$ denotes an intermediate solution state. The quantities $v_{i+1/2,k}^n$ and $\Delta U_{i+1/2,k}^n$ appearing in [31] are the local average Courant–Friedrichs–Lewy (CFL) number and solution jump vector associated with the kth elemental wave of the ith approximate Riemann problem posed between the ith and ith + 1 nodes of the spatial grid. They may be related to the eigenvalues and eigenvectors of the Jacobian of the homogeneous flux vector $J = \partial F/\partial U$ by employing Roe's approximate Riemann solver. The CFL numbers and solution jump vectors can be defined by

[33] $\quad v_{i+1/2,k}^n = \dfrac{\Delta t'' \lambda_{i+1/2,k}^n}{\Delta x_{i+1/2}}$

[34] $\quad \Delta U_{i+1/2,k}^n = \alpha_{i+1/2,k}^n e_{i+1/2,k}^n$

with $\Delta x_{i+1/2} = x_{i+1} - x_i$ and where $\lambda_{i+1/2,k}^n$ and $e_{i+1/2,k}^n$ are the kth eigenvalue and eigenvector of the flux Jacobian evaluated at an appropriate average state $U_{i+1/2}^n$. The variable $\alpha_{i+1/2,k}^n$ is the strength of the kth elemental wave. The eigenvalues of the Jacobian $J = \partial F/\partial U$ are given by

[35] $\quad \lambda_{i+1/2,1}^n = u_{i+1/2}^n - a_{i+1/2}^n, \qquad \lambda_{i+1/2,2}^n = u_{i+1/2}^n, \qquad \lambda_{i+1/2,3}^n = u_{i+1/2}^n + a_{i+1/2}^n$

and the eigenvectors can be written as

[36] $\quad e_{i+1/2,1}^n = \begin{bmatrix} 1 \\ u_{i+1/2}^n - a_{i+1/2}^n \\ h_{i+1/2}^n - u_{i+1/2}^n a_{i+1/2}^n \end{bmatrix}, \qquad e_{i+1/2,3}^n = \begin{bmatrix} 1 \\ u_{i+1/2}^n + a_{i+1/2}^n \\ h_{i+1/2}^n + u_{i+1/2}^n a_{i+1/2}^n \end{bmatrix}$

[37] $\quad e_{i+1/2,2}^n = \begin{bmatrix} 1 \\ u_{i+1/2}^n \\ h_{i+1/2}^n - \dfrac{\rho_{i+1/2}^n (a_{i+1/2}^n)^2}{\left(\dfrac{\partial p}{\partial e}\right)_{i+1/2}^n} \end{bmatrix}$

where $a_{i+1/2}^n$ is the local average state sound speed and

$$h = e + \frac{p}{\rho} + \frac{u^2}{2}$$

is the specific enthalpy. Note that for polytropic gases,

$$\frac{\partial p}{\partial e} = (\gamma - 1)\rho$$

and therefore,

$$h - \frac{\rho a^2}{\partial p / \partial e} = \frac{u^2}{2}$$

Using the condition

$$\Delta U_{i+1/2}^n = U_{i+1}^n - U_i^n = \sum_k \alpha_{i+1/2,k}^n e_{i+1/2,k}^n$$

it is possible to relate the elemental wave strengths to the average state values of the primitive variables $\rho_{i+1/2}^n$, $u_{i+1/2}^n$, $e_{i+1/2}^n$, $p_{i+1/2}^n$, $a_{i+1/2}^n$, and $h_{i+1/2}^n$ and the solution jumps

$$\Delta \rho_{i+1/2}^n = \rho_{i+1}^n - \rho_i^n, \qquad \Delta u_{i+1/2}^n = u_{i+1}^n - u_i^n, \qquad \Delta p_{i+1/2}^n = p_{i+1}^n - p_i^n$$

The resulting expressions are

$$[38] \quad \alpha_{i+1/2,1}^n = \frac{1}{2(a_{i+1/2}^n)^2} [\Delta p_{i+1/2}^n - \rho_{i+1/2}^n a_{i+1/2}^n \Delta u_{i+1/2}^n]$$

$$[39] \quad \alpha_{i+1/2,2}^n = \Delta \rho_{i+1/2}^n - \frac{\Delta p_{i+1/2}^n}{(a_{i+1/2}^n)^2}$$

$$[40] \quad \alpha_{i+1/2,3}^n = \frac{1}{2(a_{i+1/2}^n)^2} [\Delta p_{i+1/2}^n + \rho_{i+1/2}^n a_{i+1/2}^n \Delta u_{i+1/2}^n]$$

In deriving these wave strengths, it has been assumed that linearized approximations such as

$$\Delta(\rho u)_{i+1/2}^n = \rho_{i+1/2}^n \Delta u_{i+1/2}^n + u_{i+1/2}^n \Delta \rho_{i+1/2}^n$$

apply in the more general case where the solution jumps are large.

For polytropic gases obeying the ideal equation of state, Roe (39) has constructed approximate Riemann problem solutions and shown that the appropriate average state $U_{i+1/2}^n$ should be defined as follows:

$$[41] \quad \rho_{i+1/2}^n = \sqrt{\rho_{i+1}^n \rho_i^n}$$

$$[42] \quad Z_{i+1/2}^n = \frac{\sqrt{\rho_{i+1}^n} Z_{i+1}^n + \sqrt{\rho_i^n} Z_i^n}{\sqrt{\rho_{i+1}^n} + \sqrt{\rho_i^n}}, \qquad Z = u, e, \text{ and } h$$

$$[43] \quad p_{i+1/2}^n = \rho_{i+1/2}^n \left[h_{i+1/2}^n - e_{i+1/2}^n - \frac{1}{2} (u_{i+1/2}^n)^2 \right]$$

$$[44] \quad a_{i+1/2}^n = \left\{ (\gamma - 1) \left[h_{i+1/2}^n - \frac{1}{2} (u_{i+1/2}^n)^2 \right] \right\}^{1/2}$$

These averages guarantee conservation and afford the difference scheme excellent shock-capturing attributes (using the preceding definition of the average state, the approximate Riemann solution is exact for the case of a single discontinuity). Glaister (47) has since extended Roe's approximate solution to the more general case of equilibrium real-gas equations of state that have the form $p = p(\rho, e)$. In this case, the preceding averages for ρ, u, e, h, and p given by [41]–[43] are still applicable, but additional relations are required for determining local average-state values of the partial derivatives of the pressure with respect to the density and internal energy and for evaluating the average-state sound speed. Glaister's proposed averages for $\partial p / \partial \rho$ and $\partial p / \partial e$ are

$$[45] \quad \left. \frac{\partial p}{\partial \rho} \right)_{i+1/2}^n = \begin{cases} \frac{1}{2\Delta \rho_{i+1/2}^n} ([p(\rho_{i+1}^n, e_{i+1}^n) + p(\rho_{i+1}^n, e_i^n)] - [p(\rho_i^n, e_{i+1}^n) + p(\rho_i^n, e_i^n)]), & \Delta \rho_{i+1/2}^n \neq 0 \\ \frac{1}{2} \left[\left. \frac{\partial p}{\partial \rho} \right)_{i+1}^n + \left. \frac{\partial p}{\partial \rho} \right)_i^n \right], & \Delta \rho_{i+1/2}^n = 0 \end{cases}$$

$$[46] \quad \left(\frac{\partial p}{\partial e}\right)^n_{i+1/2} = \begin{cases} \frac{1}{2\Delta e^n_{i+1/2}} ([\, p(\rho^n_{i+1}, e^n_{i+1}) + p\,(\rho^n_{i+1}, e^n_i)] - [\, p(\rho^n_i, e^n_i) + p(\rho^n_i, e^n_i)]), & \Delta e^n_{i+1/2} \neq 0 \\[2mm] \frac{1}{2} \left[\left(\frac{\partial p}{\partial e}\right)^n_{i+1} + \left(\frac{\partial p}{\partial e}\right)^n_i \right], & \Delta e^n_{i+1/2} = 0 \end{cases}$$

and a is then specified using [14] by the expression

$$[47] \quad a^n_{i+1/2} = \left[\left(\frac{\partial p}{\partial \rho}\right)^n_{i+1/2} + \frac{p^n_{i+1/2}}{(\rho^n_{i+1/2})^2} \left(\frac{\partial p}{\partial e}\right)^n_{i+1/2} \right]^{1/2}$$

Although other averages have been proposed, see for example Liou *et al.* (48), this choice of averaging has been demonstrated to provide accurate solutions in a relatively efficient manner.

The higher order flux-differencing scheme of Roe is a *smart* solution adaptive method that provides improved numerical accuracy and monotonic or oscillation-free solutions by having difference coefficients that depend on the local solution at each time step. The underlying constant-coefficient or *unlimited* scheme is a combination of the second-order schemes of Lax and Wendroff (49) (central differences) and Warming and Beam (50) (upwind differences). Flux limiters are employed to limit the magnitude of the second-order antidiffusive fluxes and reduce the scheme to the first-order fully upwind method of Cole and Murman (51) at local extrema of the solution. In the case of linear and nonlinear scalar homogeneous hyperbolic conservation laws and linear systems of homogeneous conservation laws, the resulting *nonlinear* scheme is TVD (37, 38), which guarantees that the scheme is monotonicity preserving. In the more general case of nonlinear inhomogeneous systems as given by [1], numerical experiments provide evidence that Roe's flux-limited scheme has good shock-capturing capabilities. The term "higher order" is applied to Roe's method to indicate that the formal accuracy of the scheme with uniform computational domain is second order for regions where the solution is smooth (i.e., almost everywhere), but reduces to first order at extrema. Note that in the difference scheme of [30]–[32], the source terms of [1] are integrated by using a second-order Runge–Kutta or predictor corrector explicit time-stepping procedure. This provides second-order accuracy and makes the integration of the inhomogeneous terms consistent with the Roe-method time differencing of the homogeneous terms.

Following Sweby (46) the flux limiters $\phi^n_{i+1/2,k}$ of [31] are defined to be functions of the local antidiffusive flux ratios. van Leer's flux limiter

$$[48] \quad \phi^n_{i+1/2,k} = \begin{cases} 0, & v^n_{i+1/2,k} > 0, \quad b^n_{i,k} \leq 0 \\[3mm] \frac{2b^n_{i,k}}{1 + b^n_{i,k}}, & v^n_{i+1/2,k} > 0, \quad b^n_{i,k} \leq 0 \\[3mm] 0, & v^n_{i+1/2,k} > 0, \quad b^n_{i+1,k} \leq 0 \\[3mm] \frac{2}{1 + b^n_{i+1,k}}, & v^n_{i+1/2,k} < 0, \quad b^n_{i+1,k} > 0 \end{cases}$$

is used for the $k = 1$ and 3 characteristic fields, and the *superbee* limiter of Roe

$$[49] \quad \phi^n_{i+1/2,k} = \begin{cases} 0, & v^n_{i+1/2,k} > 0, \quad b^n_{i,k} \leq 0 \\[3mm] \max(\min(1, 2b^n_{i,k}), \min(2, b^n_{i,k})), & v^n_{i+1/2,k} > 0, \quad b^n_{i,k} > 0 \\[3mm] 0, & v^n_{i+1/2,k} > 0, \quad b^n_{i+1,k} \leq 0 \\[3mm] \max\left[\min\left(1, \frac{2}{b^n_{i+1,k}}\right), \min\left(2, \frac{1}{b^n_{i+1,k}}\right) \right], & v^n_{i+1/2,k} > 0, \quad b^n_{i+1,k} > 0 \end{cases}$$

is used for the $k = 2$ characteristic field. The latter more compressive limiter improves the sharpness of contact surfaces. The flux ratio $b^n_{i,k}$ is given by the ratio of the antidiffusive fluxes

[50] $b_{i,k}^{n} = \dfrac{|v_{i-1/2,k}^{n}| \, (1 - |v_{i-1/2,k}^{n}|) \, (\Delta U_{i-1/2,k}^{n} \cdot N_{U_*})}{|v_{i+1/2,k}^{n}| \, (1 - |v_{i+1/2,k}^{n}|) \, (\Delta U_{i+1/2,k}^{n} \cdot N_{U_k})}$

where N_{U_k} are normalization row vectors. In the present alogirthm, $N_{U_k} = [1, 0, 0]$ for $k = 1, 2,$ and 3.

The time-marching procedure represented by [30]–[32] is conditionally stable. The CFL criterion

[51] $\Delta t^{n} \langle \; \min_{i} \; \dfrac{\Delta x_{i+1/2}}{|u_{i}^{n}| + a_{i}^{n}}$

is used to restrict the magnitude of the time increment and thereby ensure stability and convergence of the numerical solutions.

It is also necessary to modify the finite-difference scheme near sonic points in order that the scheme be entropy-satisfying and converge to the correct physical solution. In particular, the inviscid flux functions associated with nonlinear characteristic fields 1 and 3 must be augmented to prevent the formation of *expansion* shocks. A variant of the entropy fix suggested by Roe and Pike (40) is employed. Consider elemental wave 1. A wave spreading parameter for this wave is defined to be

[52] $\delta_{i+1/2,1}^{n} = 2[\lambda_{i+1/2,1}^{n} - (u_{i}^{n} - a_{i}^{n})]$

If $\lambda_{i+1/2,1}^{n} - 1/2\delta_{i+1/2,1}^{n} < 0$ and $\lambda_{i+1/2,1}^{n} + 1/2\delta_{i+1/2,1}^{n} > 0$, then the flux limiter $\phi_{i+1/2,1}^{n}$ is set to zero and the first-order flux jump is split into two components; that is,

[53] $\dfrac{1}{2} (v_{i+1/2,1}^{n} - |v_{i+1/2,1}^{n}|) \, \Delta U_{i+1/2,1}^{n}$

is replaced by

[54] $\dfrac{f}{2} (v_{i+1/2,1}^{n+} - |v_{i+1/2,1}^{n+}|) \, \Delta U_{i+1/2,1}^{n} + \dfrac{(1-f)}{2} (v_{i+1/2,1}^{n-} - |v_{i+1/2,1}^{n-}|) \, \Delta U_{i+1/2,1}^{n}$

where

[55] $v_{i+1/2,1}^{n+} = \dfrac{1}{2}\left(\lambda_{i+1/2,1}^{n} + \dfrac{1}{2}\delta_{i+1/2,1}^{n}\right), \; v_{i+1/2,1}^{n-} = \dfrac{1}{2}\left(\lambda_{i+1/2,1}^{n} - \dfrac{1}{2}\delta_{i+1/2,1}^{n}\right)$

and

[56] $f = \dfrac{1}{2} + \dfrac{\lambda_{i+1/2,1}^{n}}{\delta_{i+1/2,1}^{n}}$

A similar procedure is required for the $k = 3$ nonlinear characteristic field.

5.2. Solution algorithm for nonequilibrium gas flows

For the case of the nonequilibrium thermodynamic model, Roe-method solutions of [1] coupled with the additional species concentration and vibrational energy conservation equations of [15] are required. In this work, these two subsystems defining the complete solution $\mathscr{U}(x, t) = \mathscr{U}(U(x, t), W(x, t))$ are not integrated in a directly coupled simultaneous fashion. Instead, two alternate gas dynamic and thermodynamic subsystems are defined and the resulting subsystems are then integrated in a time-lagged decoupled manner. This marching algorithm may be defined as follows. Given a solution $\mathscr{U}(x, t_0)$ of [1] and [15] at time t_0, an approximate solution at some later time $t_0 + \Delta t$, where Δt is a small time increment, is obtained by first solving a frozen flow or gas dynamic initial value problem defined by

[57] $\dfrac{\partial}{\partial t}(\hat{U}) + \dfrac{\partial}{\partial x}[\hat{F}(\hat{U})] = \hat{A}(\hat{U}) + \hat{S}(\hat{U}), \qquad t_0 < t \leqslant t_0 + \Delta t$

[58] $\hat{U}(x, t_0) = \hat{U}(\mathscr{U}(x, t_0)) = \hat{U}(U(x, t_0), W(x, t_0))$

and then solving a nonequilibrium thermodynamic initial value problem defined by

[59] $\dfrac{\partial \hat{W}}{\partial t} + u\dfrac{\partial}{\partial x}[H(\hat{W})] = \hat{Q}(\hat{W}), \qquad t_0 < t \leqslant t_0 + \Delta t$

[60] $\hat{W}(x, t_0) = \hat{W}(\hat{U}(x, t_0 + \Delta t), W(x, t_0))$

where

$$[61] \quad \hat{U} = \begin{bmatrix} \rho \\ \rho u \\ \rho\left(\dfrac{p}{\gamma - 1} + e_v + \dfrac{1}{2}u^2\right) \\ \rho\gamma \\ \rho R \\ \rho e_v \end{bmatrix} , \quad \hat{W} = \begin{bmatrix} c_i \\ \vdots \\ c_N \\ c_1 e_{v_1} \\ \vdots \\ c_N e_{v_N} \\ \displaystyle\sum_{s=1}^{N} \left[\dfrac{c_s R_s}{(\gamma_s - 1)}T + c_s e_{v_s}\right] + \dfrac{1}{2}u^2 \end{bmatrix}$$

$$[62] \quad \hat{F} = \begin{bmatrix} \rho u \\ \rho u^2 + p \\ \rho u \left(\dfrac{\gamma p}{(\gamma - 1)\rho} + e_v + \dfrac{1}{2}u^2\right) \\ \rho u\gamma \\ \rho u R \\ \rho u e_v \end{bmatrix} , \quad \hat{A} = \begin{bmatrix} -\rho u\dfrac{1}{A}\dfrac{dA}{dx} \\ -\rho u^2\dfrac{1}{A}\dfrac{dA}{dx} \\ -\rho u\left(\dfrac{\gamma p}{(\gamma - 1)\rho} + e_v + \dfrac{1}{2}u^2\right)\dfrac{1}{A}\dfrac{dA}{dx} \\ -\rho u\gamma\dfrac{1}{A}\dfrac{dA}{dx} \\ -\rho u R\dfrac{1}{A}\dfrac{dA}{dx} \\ -\rho u e_v\dfrac{1}{A}\dfrac{dA}{dx} \end{bmatrix}$$

$$[63] \quad \hat{S} = \begin{bmatrix} 0 \\ F_{wall} + F_{loss} \\ Q_{wall} \\ 0 \\ 0 \\ 0 \end{bmatrix} , \quad H = \begin{bmatrix} c_1 \\ \vdots \\ c_N \\ c_1 e_{v_1} \\ \vdots \\ c_N e_{v_N} \\ 0 \end{bmatrix} , \quad \hat{Q} = \begin{bmatrix} w_1 \\ \vdots \\ w_N \\ c_1 q_1 + \beta_1 w_1 e_{v_1} \\ \vdots \\ c_N q_N + \beta_N W_N e_{v_N} \\ -\displaystyle\sum_{s=1}^{N} w_s \Delta h_{f_s}^0 \end{bmatrix}$$

The approximate solution at $t_0 + \Delta t$ is then given by

$$[64] \quad \mathcal{U}(x, t_0 + \Delta t) \approx \mathcal{U}(x, t_0 + \Delta t), \hat{W}(x, t_0 + \Delta t))$$

A solution for all time $t > t_0$ may be obtained by repeating the preceding two-step algorithm and, in the limit of vanishing Δt, this solution should converge to the exact solution of [1] and [15].

The six-component subsystem of [57] has been derived by employing a *frozen flow* assumption and setting the finite-rate thermodynamic source terms of [1] to zero. Under this assumption, the behaviour of the gaseous mixture is essentially that of a polytropic (thermally and calorically perfect) gas, except that the specific heat ratio and gas constant may vary throughout the

flow field and a portion of the internal energy is locked in the vibrational modes. The last three equations of the gas dynamic subsystem are introduced to include these effects and describe changes in the quantities γ, R, and e_v, which, in the frozen-flow limit, are merely convected with the flow. Note that the solution of [57] updates the mixtures gas dynamic flow properties (e.g., ρ, u, e, e_v, p, etc. . .) but does not alter the individual species mass fractions or vibrational energies.

The multicomponent N-species nonequilibrium thermodynamic subsystem represented by [59] has been derived by assuming that the velocity and density distributions are known and fixed. This set describes the time rate of change of the species mass fractions and vibrational energies and the total internal energy of the mixture. It includes the source terms neglected in the derivation of [57]. The primitive variables, c_s, e_{v_s}, and T, and consequently e, e_v, p, and the other thermodynamic properties, are all updated by solving the thermodynamic subsystem. However, ρ and u remain unchanged.

The preceding decoupled solution procedure is similar in spirit to the techniques put forward by Glaz, *et al.* (52) and Ben-Artzi (53), and the resulting subsystems resemble the decoupled equation sets that may be obtained by using the equation-partitioning procedure suggested by Yee and Shinn (54). The term "partially decoupled" is applied herein to distinguish the current method from fully coupled algorithms, which at each level in a marching procedure solve all of the conservation equations together in a single step, and loosely coupled or chemistry-split techniques, which at each level decouple the gas dynamic and finite-rate thermodynamic equations and solve the two sets separately in a two-stage process (54).

Unlike fully coupled methods, the present alternative provides a distinct separation of the gas dynamic and finite-rate models. As a consequence, one solver can be developed for [57] and used to predict the flow of many different nonequilibrium gaseous mixtures. Mixture-specific solvers are only required for [59]. This simplifies computer program development and can make the solution algorithm more versatile than many fully coupled techniques.

The partial-decoupling approach differs from loosely coupled or chemistry-split methods because the decoupling procedure readily permits the use of the eigenvalues and eigenvectors of the complete system in the evaluation of the numerical fluxes of each subsystem. Loosely coupled methods usually employ the eigenvalues and eigenvectors of each decoupled subsystem. It is believed that the use of the eigenvalues and eigenvectors of the full equations enhances the coupling between the decoupled equation sets and thereby improves numerical solution quality (54).

Letting $\mathcal{U}_i^n$ be the numerical approximation of the solution to [1] and [15] at $x = x_i$ and $t = t^n$, the solution at subsequent time levels is obtained by employing the partial-decoupling procedure described above and applying explicit and semi-implicit versions of Roe's method to the gas dynamic and thermodynamic subsystems, respectively. The complete algorithm can be defined by

$$[65] \quad \mathcal{U}_i^{n+2} = \mathcal{L}_{\hat{U}}^{\Delta t} \, \mathcal{L}_{\hat{W}}^{2\Delta t} \, \mathcal{L}_{\hat{U}}^{\Delta t} \, \mathcal{U}_i^n$$

where the solution operator $\mathcal{L}_{\hat{U}}^{\Delta t} \, u_i^h = \mathcal{U}(\widetilde{\hat{U}_i^{n+1}}, \hat{W}_i^n)$ is represented by

$$[66] \quad \hat{U}_i^{\widetilde{n+1}} = \hat{U}_i^n + \Delta \hat{U}_i^{\tilde{n}} = \hat{U}_i^n + \Delta t^n (\hat{A}_i^n + \hat{S}_i^n) - \frac{1}{2} \sum_{k=1}^{6} \{ [(v_{i+1/2,k}^n - |v_{i+1/2,k}^n|)$$

$$+ \phi_{i+1/2,k}^n |(1 - |v_{i+1/2,k}^n|)] \Delta \hat{U}_{i+1/2,k}^n + [(v_{i-1/2,k}^n + |v_{i-1/2,k}^n|) - \phi_{i-1/2,k}^n |(1 - |v_{i-1/2,k}^n|)] \Delta \hat{U}_{i-1/2,k}^n \}$$

$$[67] \quad \hat{U}_i^{\widetilde{n+1}} = \hat{U}_i^n + \Delta \hat{U}_i^{\tilde{n}} = \hat{U}_i^{\widetilde{n+1}} + \frac{1}{2} \Delta t^n (\hat{A}_i^{\widetilde{n+1}} - \hat{A}_i^n + \hat{S}_i^{\widetilde{n+1}} - \hat{S}_i^n)$$

and the solution operator $\mathcal{L}_{\hat{W}}^{\Delta t} \, \mathcal{U}_i^n = \mathcal{U}(\hat{U}_i^n, \widetilde{\hat{W}_i^{n+1}})$ is given by

$$[68] \quad \left[I - \theta \Delta t^n \frac{\partial \hat{Q}}{\partial \hat{W}})_i^n \right] \left(\hat{W}_i^{\widetilde{n+1}} - \hat{W}_i^n \right) = \left[I - \theta \Delta t^n \frac{\partial \hat{Q}}{\partial \hat{W}})_i^n \right] \Delta \hat{W}_i^{\tilde{n}} = \Delta t^n \hat{Q}_i^n - \frac{1}{2} \sum_{k=1}^{2N+1} \{ (\omega_{i+1/2}^n - |\omega_{i+1/2}^n|)$$

$$+ \psi_{i+1/2,k}^n |\omega_{i+1/2}^n|(1 - |\omega_{i+1/2}^n|)] \Delta H_{i+1/2,k}^n + [(\omega_{i-1/2}^n + |\omega_{i-1/2}^n|) - \psi_{i-1/2,k}^n |\omega_{i-1/2}^n|(1 - |\omega_{i-1/2}^n|)] \Delta H_{i-1/2,k}^n \}$$

and where $\Delta \hat{U}_i^{\tilde{n}} = \hat{U}_i^{\widetilde{n+1}} - \hat{U}_i^n$, $\Delta \hat{U}_i^{\tilde{n}} = \hat{U}_i^{\widetilde{n+1}} - \hat{U}_i^n$, $\Delta \hat{W}_i^{\tilde{n}} = \hat{W}_i^{\widetilde{n+1}} - \hat{W}_i^n$, and $\hat{U}_i^{\widetilde{n+1}}$, $\hat{U}_i^{\widetilde{n+1}}$, and $\hat{W}_i^{\widetilde{n+1}}$ denote intermediate solution states.

The solution of the frozen-flow gas dynamic subsystem [57] is provided by the difference scheme of [66] and [67]. As was the case for the solution of the hyperbolic conservation laws of gases obeying the ideal and equilibrium *real-gas* equations of state, the quantities $v_{i+1/2,k}^n$ and $\Delta \hat{U}_{i+1/2,k}^n$ appearing in these equations are again the local average CFL numbers and solution jump vectors. They are defined in terms of the eigenvalues and eigenvectors $\lambda_{i+1/2,k}^n$ and $e_{i+1/2,k}^n$ of the Jacobian matrix $\hat{J} = \partial \hat{F}/\partial \hat{U}$ evaluated at some average state and are given by

$$[69] \quad v_{i+1/2,k}^n = \frac{\Delta t^n \lambda_{i+1/2,k}^n}{\Delta x_{i+1/2}}$$

$$[70] \quad \Delta \hat{U}_{i+1/2,k}^n = \alpha_{i+1/2,k}^n \, e_{i+1/2,k}^n$$

where $\alpha_{i+1/2,k}^n$ are the wave strengths. It can be shown that the eigenvalues and eigenvectors of the flux Jacobian $\hat{J}$ of the six-component subsystem represented by [57] are

[71] $\lambda_{i+1/2,1}^n = u_{i+1/2}^n - a_{i+1/2}^n, \qquad \lambda_{i+1/2,6}^n = u_{i+1/2}^n + a_{i+1/2}^n$

[72] $\lambda_{i+1/2,2}^n = \lambda_{i+1/2,3}^n = \lambda_{i+1/2,4}^n = \lambda_{i+1/2,5}^n = u_{i+1/2}^n$

[73] $e_{i+1/2,1}^n = \begin{bmatrix} 1 \\ u_{i+1/2}^n - a_{i+1/2}^n \\ h_{i+1/2}^n - u_{i+1/2}^n a_{i+1/2}^n \\ \gamma_{i+1/2}^n \\ R_{i+1/2}^n \\ e_{v_{i+1/2}}^n \end{bmatrix}, \qquad e_{i+1/2,6}^n = \begin{bmatrix} 1 \\ u_{i+1/2}^n + a_{i+1/2}^n \\ h_{i+1/2}^n + u_{i+1/2}^n a_{i+1/2}^n \\ \gamma_{i+1/2}^n \\ R_{i+1/2}^n \\ e_{v_{i+1/2}}^n \end{bmatrix},$

[74] $e_{i+1/2,2}^n = \begin{bmatrix} 1 \\ u_{i+1/2}^n \\ \dfrac{1}{2}\left(u_{i+1/2}^n\right)^2 + e_{v_{i+1/2}}^n \\ \gamma_{i+1/2}^n \\ R_{i+1/2}^n \\ e_{v_{i+1/2}}^n \end{bmatrix}, \qquad e_{i+1/2,3}^n = \begin{bmatrix} 0 \\ 0 \\ -\dfrac{(a_{i+1/2}^n)^2}{(\gamma_{i+1/2}^n - 1)^2} \\ \gamma_{i+1/2}^n \\ 0 \\ 0 \end{bmatrix}$

[75] $e_{i+1/2,4}^n = \begin{bmatrix} 0 \\ 0 \\ 0 \\ 0 \\ R_{i+1/2}^n \\ 0 \end{bmatrix}, \qquad e_{i+1/2,5}^n = \begin{bmatrix} 0 \\ 0 \\ e_{v_{i+1/2}}^n \\ 0 \\ 0 \\ e_{v_{i+1/2}}^n \end{bmatrix}$

with

$h = \left[\dfrac{\gamma p}{(\gamma - 1)\rho}\right] + e_v + \dfrac{u^2}{2}$

An extension of Roe's approximate Riemann solver has been developed herein to specify the appropriate average state primitive variables and wave strengths used in the preceding equations. This extension of the approximate Riemann problem solution for the subsystem of [57] yields the following averages:

[76] $\quad \rho_{i+1/2}^n = \sqrt{\rho_{i+1}^n \rho_i^n}$

[77] $\quad Z_{i+1/2}^n = \dfrac{\sqrt{\rho_{i+1}^n} Z_{i+1}^n + \sqrt{\rho_i^n} Z_i^n}{\sqrt{\rho_{i+1}^n} + \sqrt{\rho_i^n}}, \qquad Z = u,\ \gamma,\ R,\ e_v,\ \text{and}\ h$

[78] $\quad a_{i+1/2}^n = \left\{ (\gamma_{i+1/2}^n - 1)\left[h_{i+1/2}^n - e_{v_{i+1/2}}^n - \dfrac{1}{2}(u_{i+1/2}^n)^2 \right] \right\}^{1/2}$

and wave strengths

[79] $\quad \alpha_{i+1/2,1}^n = \dfrac{1}{2(a_{i+1/2}^n)^2}[\Delta p_{i+1/2}^n - \rho_{i+1/2}^n a_{i+1/2}^n \Delta u_{i+1/2}^n]$

[80] $\quad \alpha_{i+1/2,2}^n = \Delta \rho_{i+1/2}^n - \dfrac{\Delta p_{i+1/2}^n}{(a_{i+1/2}^n)^2}$

[81] $\quad \alpha_{i+1/2,3}^n = \dfrac{\rho_{i+1/2}^n}{\gamma_{i+1/2}^n}\Delta\gamma_{i+1/2}^n, \qquad \alpha_{i+1/2,4}^n = \dfrac{\rho_{i+1/2}^n}{R_{i+1/2}^n}\Delta R_{i+1/2}^n, \qquad \alpha_{i+1/2,5}^n = \dfrac{\rho_{i+1/2}^n}{e_{v_{i+1/2}}^n}\Delta e_{v_{i+1/2}}^n$

[82] $\quad \alpha_{i+1/2,6}^n = \dfrac{1}{2(a_{i+1/2}^n)^2}[\Delta p_{i+1/2}^n + \rho_{i+1/2}^n a_{i+1/2}^n \Delta u_{i+1/2}^n]$

Note that the flux limiters $\phi_{i+1/2,k}^n$, which provide the difference scheme of [66] and [67] with the desirable TVD property, are evaluated similarly to the limiters used in the solution for the polytropic and equilibrium cases. The flux limiter of van Leer defined by [48] is used for the $k = 1$ and 6 characteristic fields and the superbee flux limiter of [49] is used for the $k = 2, 3, 4,$ and 5 characteristic fields. Appropriate values for the flux ratios and normalization row vectors are used. Finally, note also that the flux functions of the $k = 1$ and 6 nonlinear characteristic fields are modified by employing entropy fixes of the form given by [52]–[56].

The integration of the thermodynamic subsystem [59] is provided by the TVD semi-implicit scheme of [68]. In [68], I is the identity matrix, $\partial\hat{Q}/\partial\hat{W}$ is the source Jacobian matrix, $\omega_{i+1/2}^n$ and $\Delta H_{i+1/2,k}^n$ are the local average CFL number and solution jump vectors used in evaluating the flux functions for the species concentration and vibrational energy equations, and $\psi_{i+1/2,k}^n$ are the flux limiters. The homogeneous form of the subsystem given by [59] is essentialy a system of independent convection equations and, therefore, the numerical flux functions can be evaluated quite simply. The CFL number $\omega_{i+1/2}^n$ is given by

[83] $\quad \omega_{i+1/2}^n = \dfrac{\Delta t^n u_{i+1/2}^n}{\Delta x_{i+1/2}}$

where $u_{i+1/2}^n$ is evaluated by using [76] and [77] resulting from the extended approximate Riemann solver. This ensures that the eigenvalues and eigenvectors of the fully coupled system

are used in the computation of the flux functions of both the gas dynamic and thermodynamic subsystems. The solution jump column vectors for the $N_D = 2N + 1$ component thermodynamic subsystem are given by

[84] $\quad \Delta H_{i+1/2,k}^n = D_k \Delta H_{i+1/2}^n$

where $\Delta H_{i+1/2}^n = H_{i+1}^n - H_i^n, D_k$ is a diagonal matrix for which the elements of the diagonal are $(\delta_{1k}, \ldots, \delta_{kk}, \ldots, \delta_{N_Dk})$, and δ is the usual Kronecker delta function. Finally, the flux limiters $\psi_{i+1/2,k}^n$ for each component of the solution vector, which limit the magnitude of the antidiffusive flux in [68], are evaluated by employing the superbee formulation of [49]. The flux ratio is again defined in terms of the ratio and the antidiffusive fluxes and the normalization row vector is chosen to recover the component of the antidiffusive flux vector associated with the kth component of the solution vector $\hat{W}$. Note that entropy corrections are not required in the solution of the thermodynamic subsystem.

The stiffness of the source terms associated with the finite-rate reaction and relaxation processes of [68] force the time step sizes of explicit schemes to be excessively small and the corresponding computer times to be prohibitively large. For this reason, the source terms of the operator $\mathscr{L}_{\hat{W}}^{\Delta t}$ are integrated by using an implicit time-stepping procedure that is similar to the semi-implicit algorithms proposed by Bussing and Murman (55), Yee and Shinn (54), and Ben-Artzi (53) for the computation of chemically reacting flows. These schemes treat only the source terms implicitly. This effectively alleviates the stiff-
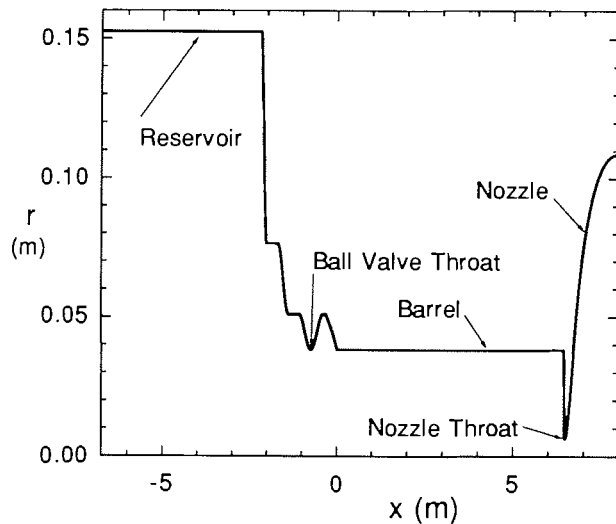
CAN. J. PHYS. VOL. 69, 1991

FIG. 2. UTIAS hypersonic impulse tunnel geometry used in numerical simulations.
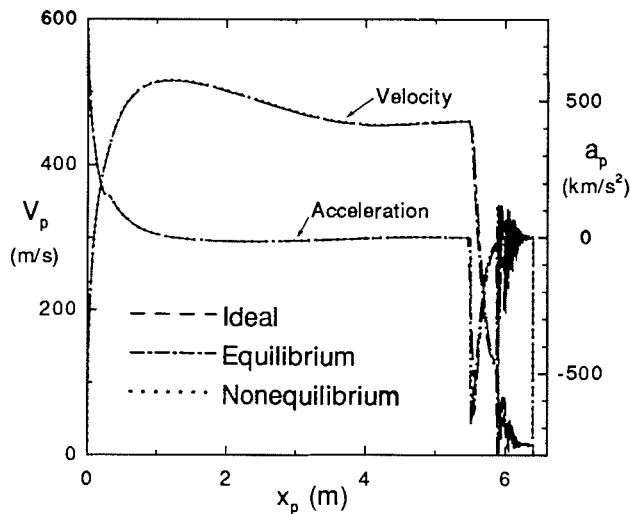

FIG. 3. Piston velocity V_p and acceleration a_p. p_{res} = 20.5 MPa, p_{brl} = 400 kPa, T_{res} = T_{brl} = 293 K, m_p = 96 g.

ness associated with the finite-rate relaxation and reaction time scales while avoiding large matrix inversions. The quantity $[I - \theta \Delta t^n (\partial \hat{Q}/\partial \hat{W})\,_j^n]$ is similar to the preconditioning matrices used by Bussing and Murman (55). The parameter θ controls the implicit time stepping. For $\theta = 0$, the time differencing is Euler explicit. For $\theta = 1$, the time differencing is Euler implicit. This value produces the most stable scheme and is appropriate for problems with extremely stiff source terms. A value of $\theta = 1/2$ produces a trapezoidal implicit time differencing that is best suited and consistent with the explicit time-differencing of the homogeneous terms. Note that the time-marching procedure represented by [66]–[68] is conditionally stable. For $\theta \geqslant 1/2$, the CFL condition [51] ensures stability and convergence.

5.3. Boundary conditions

Boundary conditions are necessary for the prescription of the numerical solutions at the extremities of the computational domains. There are two types of boundary conditions required for the hypersonic impulse tunnel simulations. Firstly, a solid-
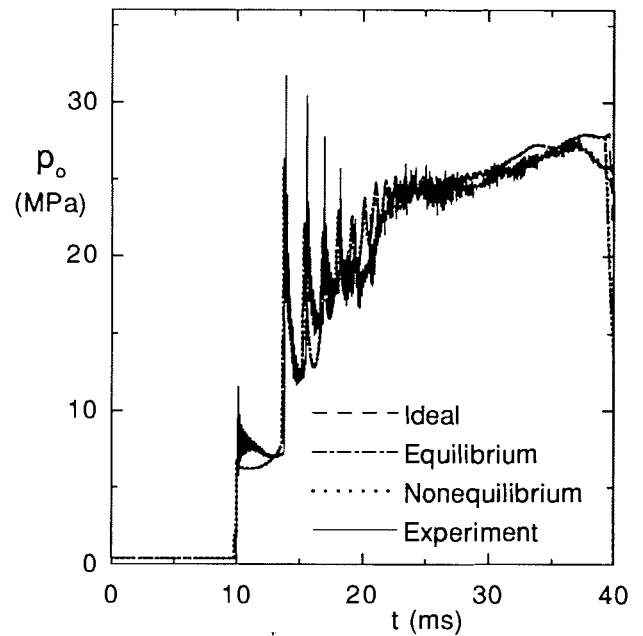
FIG. 4. Barrel end stagnation pressure p_o. p_{res} = 20.5 MPa, p_{brl} = 400 kPa, T_{res} = T_{brl} = 293 K, m_p = 96 g.

surface reflecting boundary condition is needed for the flow properties at the closed end of the reservoir and the front and back faces of the moving piston. Secondly, an outflow boundary condition is needed for the flow properties at the exit of the contoured nozzle.

Reflecting boundary conditions are applied by forcing the flow to have the velocity of the solid boundary or piston and then employing Rankine–Hugoniot and Riemann invariant relations across shocks and rarefaction waves to determine the other solution properties. For the outflow boundary condition at the nozzle exit, it is recognized that, except for very early in the tunnel operation cycle, the flow is almost always supersonic at this point and disturbances from the test section cannot propagate upstream. Simple constant extrapolation or transmissive boundary conditions (56) at the nozzle exit are therefore quite appropriate and are used here.

6. Discussion of numerical results and performance data

This section presents numerical predictions of the UTIAS–RPI hypersonic impulse tunnel performance obtained by solving the one-dimensional flow and thermodynamic model equations of Sects. 3 and 4 using the TVD numerical integration schemes described in Sect. 5. The performance of the facility is first assessed by considering its operation under two firing states that are commonly used for much of the ongoing experimental hypersonic research at UTIAS. Additional numerical results are then presented to establish more thoroughly the tunnel performance envelope and operating range.

The UTIAS–RPI impulse tunnel is generally operated with initial reservoir pressure p_{res} = 20.5 MPa, initial reservoir and barrel temperatures T_{res} = T_{brl} = 293 K, and piston mass m_p = 96 g. Different operating conditions are achieved by varying the initial barrel pressure p_{brl}. Two firing modes are employed in the majority of experiments. In one mode, p_{brl} = 400 kPa and in the other, p_{brl} = 200 kPa. Note that the firing state with the lower initial barrel pressure produces a higher stagnation enthalpy flow in the test section.
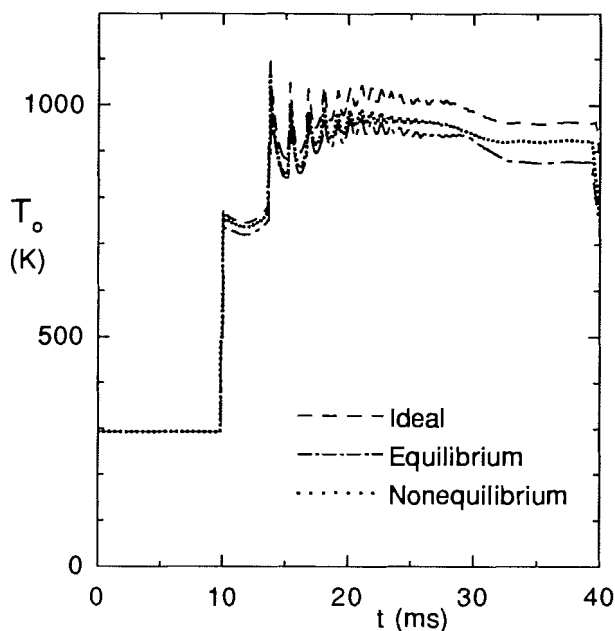
FIG. 5. Barrel end stagnation temperature T_o. $p_{res} = 20.5$ MPa, p_{brl} = 400 kPa, $T_{res} = T_{brl} = 295$ K, $m_p = 96$ g.
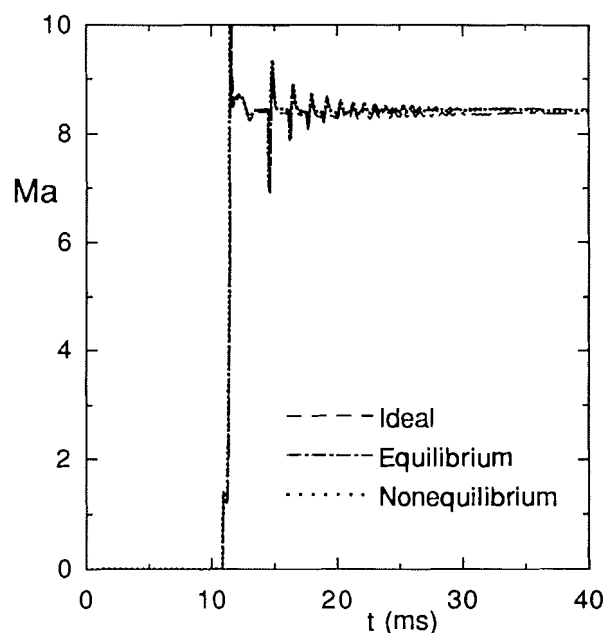

FIG. 6. Nozzle exit Mach number Ma. $p_{res} = 20.5$ MPa, p_{brl} = 400 kPa, $T_{res} = T_{brl} = 293$ K, $m_p = 96$ g.

FIG. 7. Temperature distributions in nozzle, $t = 30$ ms. $p_{res} = 20.5$ MPa, $p_{brl} = 400$ kPa, $T_{res} = T_{brl} = 293$ K, $m_p = 96$ g.

For the computations of the tunnel operation in these two modes, and indeed for all of the predictions presented in this section, the unsteady motion of the driver and working gases is solved for the entire facility between the closed end of the reservoir and the nozzle exit. The cross-sectional area function $A(x)$ used in the numerical simulations is illustrated in Fig. 2 in terms of the axial position x and local tunnel radius $r(x)$ where $A = \pi r^2$. A total of 570 spatial nodes are used to represent the discretized computational domain. Convergence tests suggest that this nodal density is sufficient as numerical errors appear to be nominally less than 3–5% when 500–600 nodes are used. Boundary-layer frictional losses and heat transfer are included with $\epsilon = 0.025$ mm. These loss effects are, however, not included in the computation of the flow in the nozzle section. This is a reasonable approximation because the flow in this section of the tunnel is definitely not fully developed. The nozzle has been specifically designed to produce a relatively large inviscid core flow with a boundary layer that is confined, for the most part, to the near wall region. A value of 0.25 is assumed for the head-loss coefficients K of the two diaphragms located just downstream of the ball valve section. Note that the diaphragm head losses are phased in during the first 5 ms after diaphragm rupture using a linear-ramping function to more accurately simulate the developing flow situation occurring in the initial stages of tunnel startup. All of the computations were performed on a Hewlett-Packard/Apollo 400s workstation. The simulations of the ideal and equilibrium gas cases required approximately 4-5 central-processing-unit hours (CPUh), whereas the nonequilibrium gas cases required about 13–14 CPUh.

The predictions of the tunnel operation with initial barrel pressures of 400 and 200 kPa are presented in Figs. 3–12. The first set of results for a barrel pressure of 400 kPa is given in Figs. 3–7, whereas the other set for a barrel pressure of 200 kPa is in Figs. 8–12. Note that the calculations were performed with the ideal, real equilibrium, and five-species four-temperature nonequilibrium gas models, and the results for these three different thermodynamic models are compared in these figures.
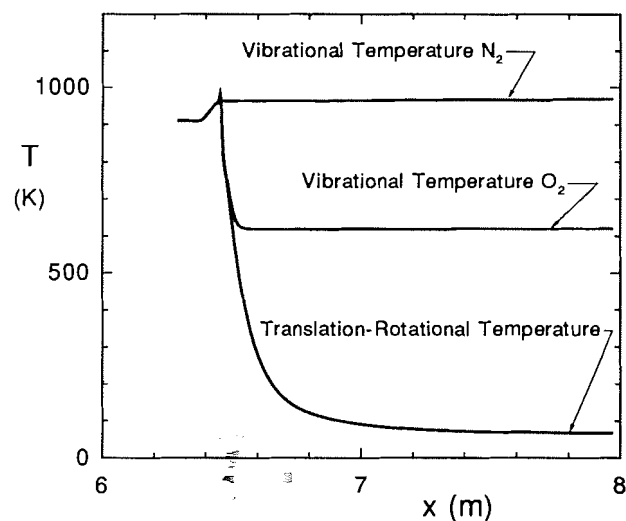
Consider first the results with $p_{brl} = 400$ kPa. The piston velocity V_p and acceleration a_p as a function of piston position in the barrel x_p are given in Fig. 3. From Fig. 3, it is clear that the piston rapidly accelerates during the first metre of travel and then is subjected to very little acceleration until the first reflected shock from the barrel end causes it to decelerate. Subsequent reflections cause further deceleration and the piston eventually comes to rest at the end of the barrel ($x_p \approx 6.7$ m). A maximum velocity of somewhere near 515 m s^{-1} and a peak acceleration approaching 760 km s^{-2} are predicted. Figure 3 also clearly illustrates that high-temperature and (or) real-gas effects have very little effect on the predicted piston motion. The piston trajectories determined using the real equilibrium and nonequilibrium gas thermodynamic models are virtually identical to the trajectory obtained using the polytropic model.
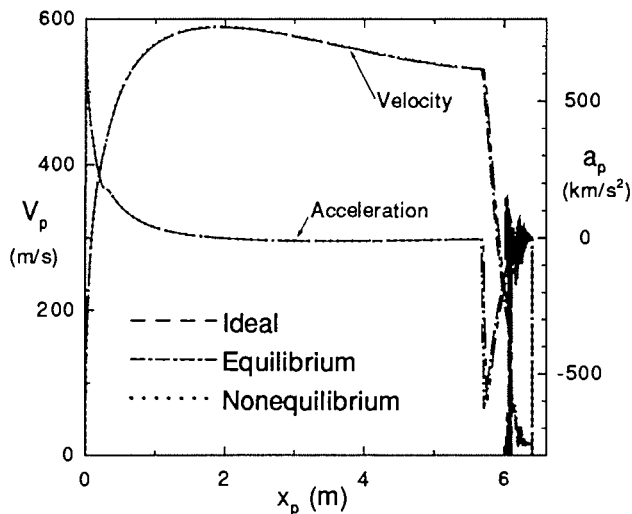
FIG. 8. Piston velocity V_p and acceleration a_p. p_{res} = 20.5 MPa, p_{brl} = 200 kPa, T_{res} = T_{brl} = 293 K, m_p = 96 g.

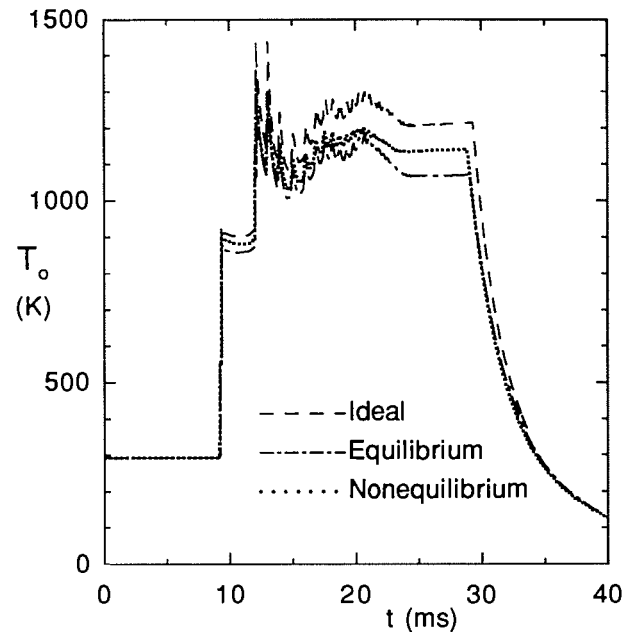FIG. 9. Barrel end stagnation pressure p_o. p_{res} = 20.5 MPa, p_{brl} = 200 kPa, T_{res} = T_{brl} = 293 K, m_p = 96 g.
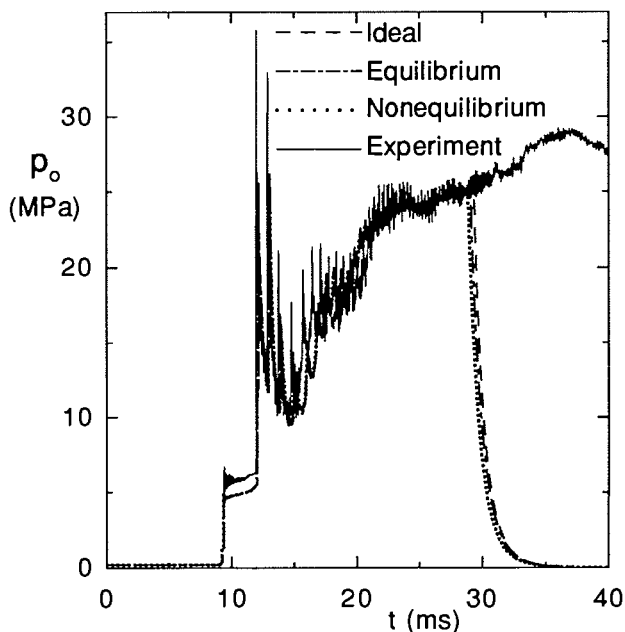
FIG. 10. Barrel end stagnation temperature T_o. p_{res} = 20.5 MPa, p_{brl} = 200 kPa, T_{res} = T_{brl} = 293 K, m_p = 96 g.

The predicted temporal variations of the stagnation pressure p_0 and temperature T_0 at the end of the barrel as the flow in the nozzle relaxes towards a steady state condition are illustrated in Figs. 4 and 5. The time $t = 0$, in these and other temporal distributions to follow, corresponds to the time when the first of the two diaphragms ruptures. The multiple shock reflections associated with the nonisentropic compression of the working gas is clearly illustrated by the successive pressure and temperature jumps in the time histories. These jumps indicate the passage of the reflected shocks between the piston front face and end of the barrel. The two sets of curves in the figures indicate that high-temperature phenomena are important in determining the nozzle flow stagnation conditions. Although there are only minor differences between the ideal, equilibrium, and nonequilibrium results for the stagnation pressures, the stagnation temperatures obtained with each thermodynamic

model are quite different. It can be seen that the predicted stagnation pressure during the period of relatively steady-state nozzle flow is between 24–27 MPa for all three thermodynamic models. This pressure begins to drop rapidly around $t = 39$ ms when the working gas is depleted and the piston comes to rest at the end of the barrel. The polytropic model provides a higher stagnation temperature than the temperatures predicted by the two real-gas models, as should be expected. The predicted ideal stagnation temperature appears to be around 980–1000 K whereas the equilibrium and nonequilibrium values are around 910–920 and 940–950 K, respectively. Note that at these stagnation temperatures, vibrational excitation of the nitrogen (N_2) and oxygen (O_2) diatomic molecules is significant, but dissociation of these species is small. The differences in the curves of Fig. 5 indicate that nonequilibrium relaxation must be considered in order to determine the stagnation temperature accurately.

As an additional comparison, an experimental stagnation pressure trace measured during a firing of the UTIAS–RPI facility with an initial barrel pressure of 400 kPa is also presented in Fig. 4. It is evident from Fig. 4 that many of the detailed features and complicated wave structure of the nonstationary flow in the tunnel, such as shock strengths and times of arrival, are correctly reproduced by the one-dimensional nonstationary flow model calculations and that the numerical predictions are in good agreement with the experimental time-history data, both qualitatively and quantitatively.

Figure 6 depicts the temporal variation of the flow Mach number Ma at the exit of the contoured nozzle. Figure 6 clearly demonstrates the establishment of steady flow in the nozzle. The exit Mach number initially oscillates about a mean value. These oscillations indicate the passage of transmitted shock waves through the nozzle and test section. A relatively steady-state nozzle flow is then achieved at about 25 ms after the first diaphragm has burst and is maintained until sometime just after the $t = 40$ ms mark. At this time, the piston has come to rest and the stagnation pressure and temperature at the nozzle entrance have dropped dramatically. This suggests a run time
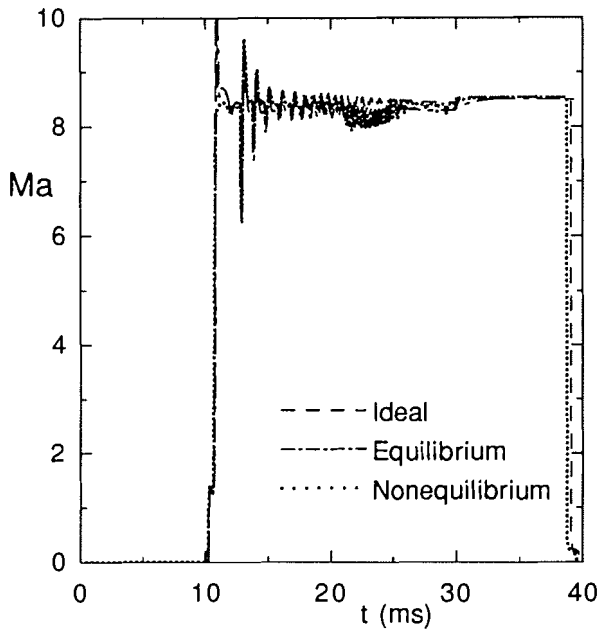
FIG. 11. Nozzle exit Mach number Ma. p_{res} = 20.5 MPa, p_{brl} = 200 kPa, T_{res} = T_{brl} = 293 K, m_p = 96 g.

FIG. 12. Temperature distributions in nozzle, t = 20 ms. p_{res} = 20.5 MPa, p_{brl} = 200 kPa, T_{res} = T_{brl} = 293 K, m_p = 96 g.

FIG. 13. Barrel end stagnation pressure p_o. p_{res} = 20.5 MPa, p_{brl} = 400 kPa, T_{res} = T_{brl} = 293 K, m_p = 96 g.

of somewhere between 15 and 17 ms for this particular mode of tunnel operation. It is interesting to note that, as mentioned in Sect. 2, the contoured nozzle employed in the present impulse tunnel configuration was built with an exit flow Mach number of 8.33 as one of the design specifications and that, for all thermodynamic models, the predicted steady-state nozzle exit Mach number is about 8.35–8.45. Note also that the numerical results show that the pressure p, temperature T, and specific heat ratio γ of the air flow at the nozzle exit are approximately 1.6–1.7 kPa, 65–75 K, and 1.4, respectively.

Plots of the spatial distributions of the vibrational temperatures of the two excited diatomic species (N_2 and O_2) and the equilibrium translational and rotational temperature at time t = 30 ms in the UTIAS–RPI tunnel from the piston front face to nozzle exit are also shown in Fig. 7. These numerical results were obtained with the nonequilibrium thermodynamic model. Note that the calculations performed show that in this operation mode dissociation/recombination effects are negligible and the principal nonequilibrium phenomenon that occurs at stagnation in the barrel is vibrational relaxation. This is as expected for these stagnation temperatures. It has long been known that typically vibrationally excited air *freezes* when it becomes moderately supersonic (18, 20) and this seems to be the case here. The distributions of Fig. 7 demonstrate that the air in the nozzle freezes somewhere close to the nozzle throat, with the nitrogen freezing first near 965 K and the oxygen following at a temperature of about 620 K. This produces a test-section flow of air with excited vibrational states and vibrational temperatures much higher than the equilibrium translational–rotational temperature of 67 K.

Figures 8–12 show the numerical predictions of the UTIAS–RPI hypersonic impulse tunnel operation with an initial barrel pressure of 200 kPa. The results are similar to those of the 400 kPa simulations, except that the maximum piston velocity is now higher and approaches 600 m s^{-1}, the stagnation pressure is around 24–25 MPa, the simulated stagnation temperatures are considerably higher ranging from 1070–1210 K, and the duration of steady nozzle flow is now reduced to about
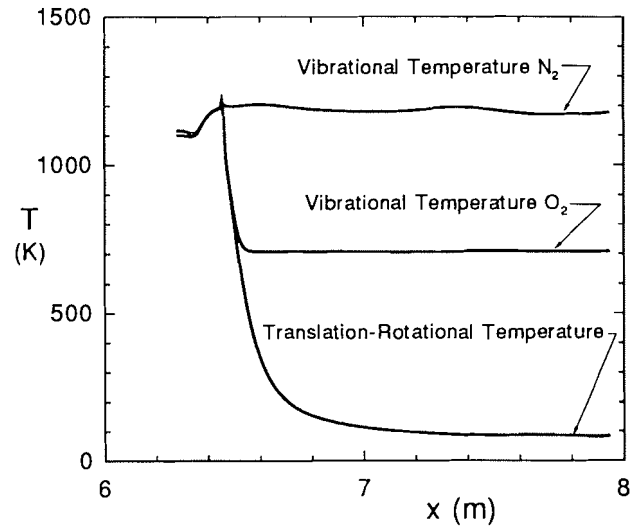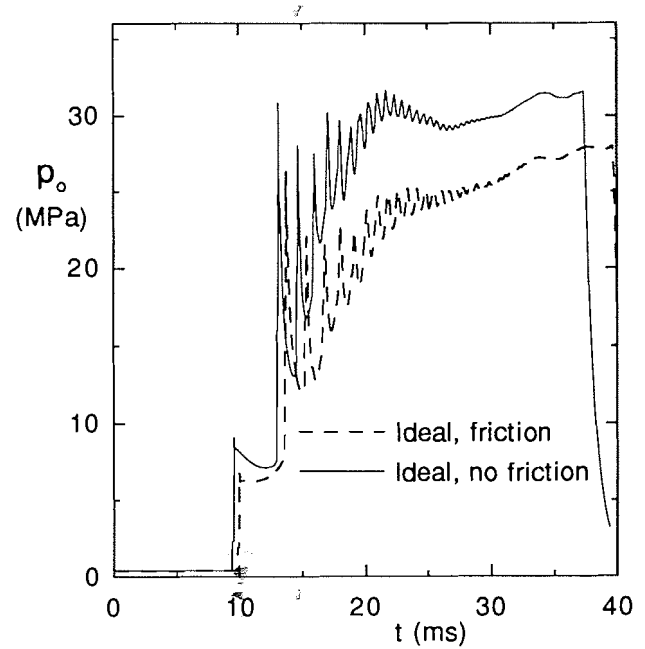
9.5 ms. Figure 9 illustrates that, except for some differences in the later stages of the tunnel operation cycle (t > 30 ms), the agreement between numerical predictions and experimental measurements of the stagnation pressure is again good. The differences after t = 30 ms can be explained as follows. The stagnation pressure ahead of the piston drops in the numerical predictions. However, this characteristic pressure drop is not observed in the experimental signature because, in this particular firing, the piston has passed by the transducer and sealed the entrance to the nozzle. Figure 12 provides further evidence that the air flow at the nozzle exit, and thus the air flow in the test section, of the UTIAS–RPI facility has considerable energy locked in the excited vibrational modes of the nitrogen and oxygen gas molecules. Vibrational temperatures at the nozzle exit of 1180 and 830 K are predicted for N_2 and O_2, respectively.
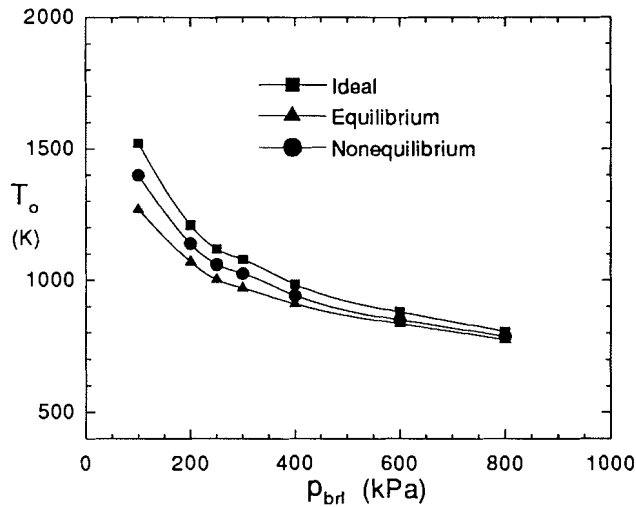
FIG. 14. Barrel end stagnation pressure T_o as a function of initial barrel pressure p_{brl}, $p_{res} = 20.5$ MPa, $T_{res} = T_{brl} = 293$ K, $m_p = 96$ g.
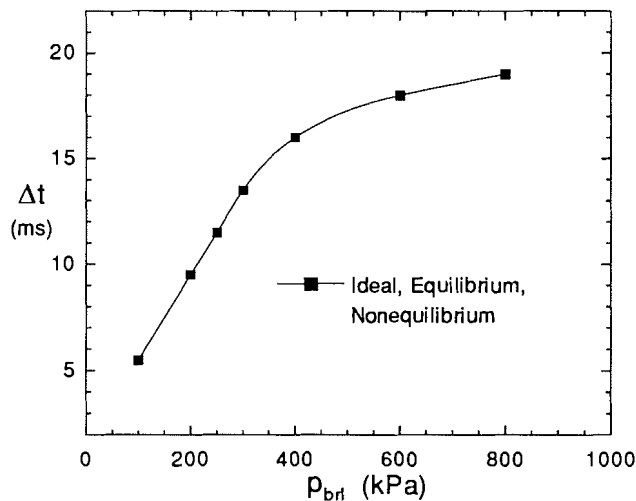

FIG. 15. Run time Δt as a function of the initial barrel pressure p_{brl}, $p_{res} = 20.5$ MPa, $T_{res} = T_{brl} = 293$ K, $m_p = 96$ g.

Note that the low-amplitude oscillatory nature of the N_2 temperature distribution of Fig. 12 in the region downstream of the throat is a consequence of the temporal variations in the stagnation conditions created by the nonisentropic compression process occurring in the barrel.

Before continuing, it is worth mentioning that the influence of boundary-layer friction and heat transfer, included in the present analysis, are important and cannot be neglected if accurate predictions of stagnation, nozzle, and test-section flow properties are desired. This is illustrated in Fig. 13 where two predictions of the ideal-gas stagnation pressure p_0 are depicted. In one case the stagnation pressure is computed with the boundary-layer losses included and in the other these effects have been omitted. It is apparent that the times of arrival and strengths of nonstationary shocks, as well as the resulting steady-state stagnation pressure, are very different for these two cases. To obtain the level of quantitative agreement between numerical predictions and experimental measurements found in Fig. 4 and 9, the incorporation of boundary-layer effects into the analysis seems to be required.
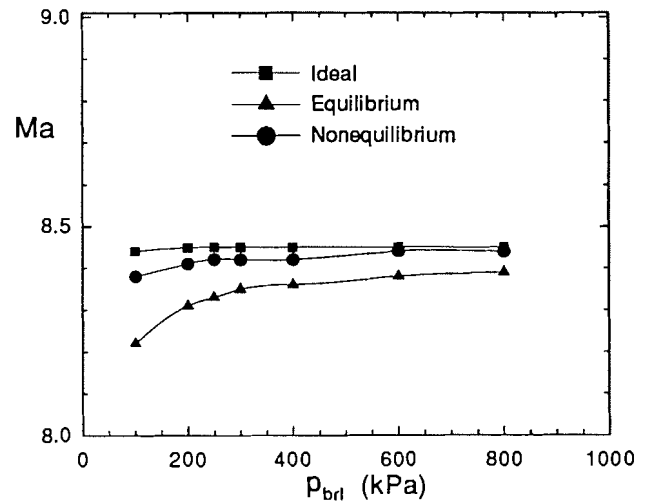

FIG. 16. Nozzle exit Mach number Ma as a function of initial barrel pressure p_{brl}, $p_{res} = 20.5$ MPa, $T_{res} = T_{brl} = 293$ K, $m_p = 96$ g.

It should also be noted that the time scales associated with the finite-rate source terms in the preceding nonequilibrium computations were approximaely 500–10 000 times smaller than the gas dynamic time scales. The semi-implicit solver of [65]–[68] effectively removed the stability constraints imposed by the finite-rate times scales and permitted the computations to be performed with the numerical time steps controlled only by the gas dynamic time scales.

The performance characteristics of the UTIAS–RPI hypersonic impulse tunnel are further illustrated by the numerical results depicted in Figs. 14–19. In these figures, the computed barrel end stagnation pressure T_0, facility run time Δt, nozzle exit flow Mach number Ma, and nozzle exit flow Reynolds number per unit length Re/L are given as functions of the initial barrel pressure p_{brl}, piston mass, m_p, and initial barrel temperature T_{brl}. The results are again given for all three thermodynamic models.

In Figs. 14–17, the effects of varying the initial barrel pressure from 100 to 800 kPa with $p_{res} = 20.5$ MPa, $T_{res} = T_{brl} = 293$ K, and $m_p = 96$ g all fixed are explored. Figure 14 shows that by reducing the barrel pressure higher stagnation temperatures approaching 1500 K are possible. However, Fig. 15 shows that these moderate increases in stagnation enthalpy are offset by a corresponding decrease in the facility run time, which may be detrimental to experiments in many cases. Note that the run times are virtually the same for all three thermodynamic models. Figure 16 illustrates that the test-section flow Mach number is rather insensitive to the initial barrel pressure. This should be expected for it depends primarily on the exit to throat area ratio. Although not shown, the stagnation pressure was also found to be insensitive to initial barrel pressure. Values for p_0 were found to be around 24–27 MPa for all of the operating conditions considered. Finally, Fig. 17 presents the range of nozzle-exit or test-section flow Reynolds number per unit length that may be achieved with the UTIAS–RPI tunnel. The Reynolds number varies from 10^7 to 5×10^7 m^{-1}, which suggests that, depending on the model size and orientation in the test section, fully laminar, transitional, and even fully turbulent boundary-layers may be obtained.

For many experimental programs, higher test-section stagnation temperatures are desired. Two of the possible and more
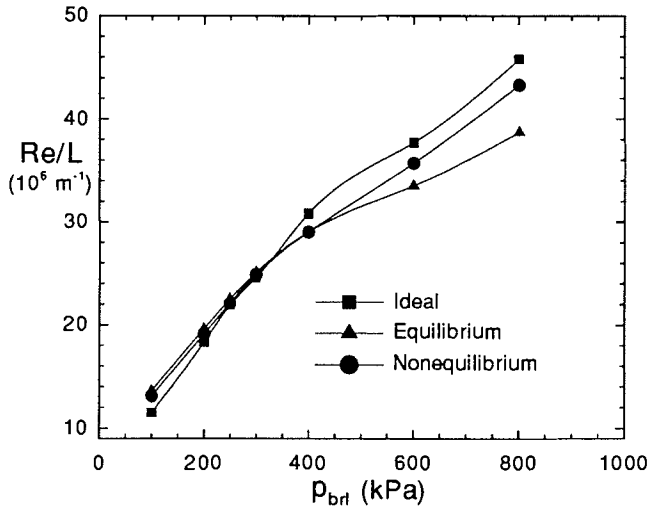
FIG. 17. Nozzle exit Reynolds number per unit length Re/L as a function of the initial barrel pressure p_{brl}, $p_{res} = 20.5$ MPa, $T_{res} = T_{brl} = 293$ K, $m_p = 96$ g.
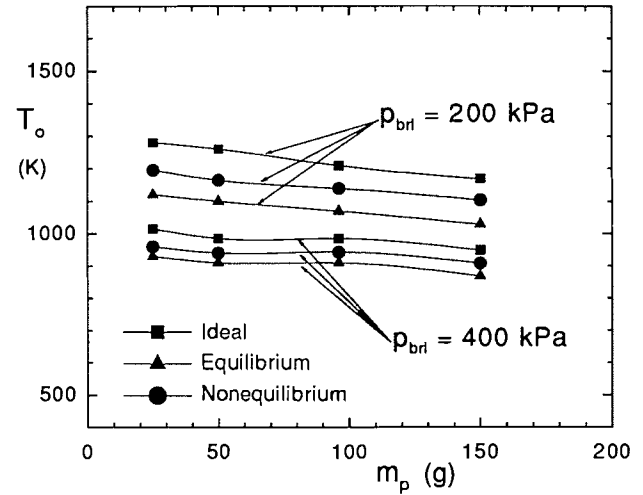

FIG. 18. Barrel end stagnation pressure T_o as a function of the piston mass m_p, $p_{res} = 20.5$ MPa, $p_{brl} = 200$ and 400 kPa, $T_{res} = T_{brl} = 293$ K.
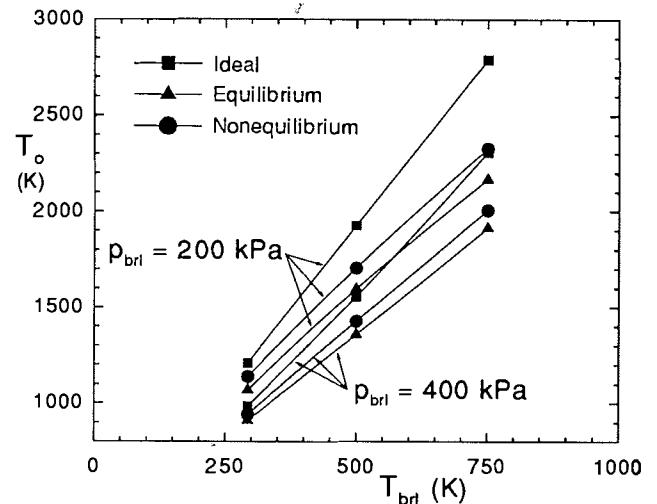

FIG. 19. Barrel end stagnation pressure T_o as a function of initial barrel temperature T_{brl}, $p_{res} = 20.5$ MPa, $P_{brl} = 200$ and 400 kPa, $T_{res} = 293$ K, $m_p = 96$ g.

practical avenues for achieving higher temperatures are to redesign and reduce the piston mass by employing lightweight high strength materials or to preheat the working gas in the barrel before diaphragm rupture. The effects of varying the piston weight and initial barrel temperature with $p_{res} = 20.5$ MPa, $T_{res} = 293$ K, and $p_{brl} = 200$ and 400 kPa are shown in Figs. 18 and 19. It should be obvious from Fig. 18 that changing the piston mass has little effect. Even the reduction of the piston mass by as much as 75% provides a corresponding increase in the predicted stagnation temperatures of only 40 K. On the other hand, Fig. 19 shows that preheating the barrel gases is more worthwhile. An increase in the initial barrel temperature of 200 K can provide a corresponding increase in the stagnation pressure of up to 400 K. It should, however, be noted that preheating the working gas does reduce the run time. With $p_{brl} = 200$ kPa, the run time Δt was found to decrease almost linearly with temperature from about 10 ms at $T_{brl} = 293$ K down to 5 ms at $T_{brl} = 750$ K.

7. Concluding remarks

A quasi-one-dimensional unsteady flow analysis and TVD finite-difference solution algorithm with new numerical features have been presented for the prediction of the UTIAS–RPI hypersonic impulse tunnel operation and performance. Unlike previous studies which have generally employed quasi-steady and mostly analytic techniques, modern CFD methods are used to predict for the first time the complete unsteady behaviour of the impulse tunnel from initial startup to blow down. Furthermore, the use of polytropic gas, real equilibrium gas, and four-temperature five-species nonequilibrium gas thermodynamic models in the analysis has permitted the evaluation of high temperature effects for this experimental facility. Numerical results and comparisons to available experimental data have demonstrated the capabilities and usefulness of these modeling techniques.

Under typical operating conditions, the numerical predictions have shown that the run time for the UTIAS–RPI impulse tunnel is about 15–20 ms and that the stagnation pressure and temperature are 24–27 MPa and 1000–1200 K, respectively. Test section flow Mach and Reynolds numbers of 8.35–8.45 and 10^7 to 5×10^7 m^{-1} were found. In addition, the static

pressure and temperature in the test section were determined to be about 1.6–1.7 kPa and 65–75 K respectively. For the predicted stagnation enthalpies, it was shown that in most cases the primary high-temperature phenomenon occurring in the tunnel was vibrational excitation. The degrees of dissociation of N_2 and O_2 were found not to exceed 1/2 and 2%, respectively, even in the extreme cases considered where stagnation temperatures neared 2000 K. It was also demonstrated that vibrational excitation must be treated as a finite-rate process to obtain accurate predictions of the tunnel stagnation conditions.

Vibrational relaxation effects were also found to be of importance in the hypersonic nozzle flows of the UTIAS–RPI facility. It was shown that the air typically freezes downstream but very close to the nozzle throat and results in test-section flows with nitrogen and oxygen species having vibrational temperatures of 960–1200 K and 620–830 K, respectively. These temperatures are much higher than the predicted test-section translational-rotational temperatures and may be important in the assessment of tunnel experimental data.

One of the limitations of the UTIAS–RPI facility seems to be the rather low stagnation enthalpies that can be obtained. The present performance assessment of the impulse tunnel indicates a possible technique for extending the range of flow conditions that can be achieved in the test section. Reducing the piston weight proves to be fruitless; however, preheating of the working gas can lead to substantially higher stagnation temperatures and feasible preheating mechanisms could be examined in the future.

Acknowledgments

1. W. G. VINCENTI and C. H. KRUGER. Introduction to physical gas dynamics. R. E. Krieger Publishing, Huntington, NY. 1975.
2. J. D. ANDERSON. Modern compressible flow with historical perspective. McGraw-Hill Book Co., New York. 1982.
3. J. D. ANDERSON. Hypersonic and high temperature gas dynamics. McGraw-Hill Book Co., New York. 1989.
4. J. LUKASIEWICZ. Experimental methods of hypersonics. Marcel Dekker Inc., New York, 1973.
5. H. G. HORNUNG. Aeronaut. J. 92, 379 (1988).
6. J. L. STOLLERY, D. J. MAULL, and B. J. BELCHER. J. R. Aeronaut. Soc. 64, 24 (1960).
7. R. J. STALKER. AIAA J. 3, 1170 (1965).
8. R. J. STALKER. AIAA J. 5, 2160 (1967).
9. R. J. STALKER. Ann. Rev. Fluid Mech. 21, 37 (1989).
10. R. L. DESCHAMBAULT, R. J. HAWBOLDT, P. A. SULLIVAN, and S. MOLDER. In Proceedings of the First Canadian Symposium on Aerodynamics, Canadian Aeronautics and Space Institute, Ottawa, Canada, December 4 and 5, 1989. Canadian Aeronautics and Space Institute. 1989.
11. A. HERTZBERG. J. Aeronaut. Sci. 18, 803 (1951).
12. A. HERTZBERG. NATO AGARD Rep. 144, July 1957.
13. C. E. WITTLIFF, M. R. WILSON, and A. HERTZBERG. J. Aeronaut. Sci. 26, 219 (1959).
14. C. EVANS and F. EVANS. J. Fluid Mech. 1, 399 (1956).
15. J. L. STOLLERY and D. J. MAULL. J. Fluid Mech. 4, 650 (1958).
16. D. F. T. WINTER. J. Fluid Mech. 8, 264 (1960).
17. R. J. STALKER. National Research Council of Canada Mechanical Engineering Report MT-42, March 1961.
18. J. L. STOLLERY and J. E. SMITH. J. Fluid Mech. 13, 225 (1962).
19. B. LEMCKE. Aeronautical Research Institute of Sweden Report 90, February 1962.
20. J. L. STOLLERY and C. PARK. Imperial College of Science and Technology Aeronautics Department Report No. 115, January 1963.
21. P. A. JACOBS. ICASE Report No. 91-1, January 1991.
22. M. J. ZUCROW and J. D. HOFFMAN. Gas dynamics. Vol. 1. John Wiley and Sons, Toronto. 1976.
23. K. Y. ZHANG and J. J. GOTTLIEB. University of Toronto Institute for Aerospace Studies Report No. 304, March 1986.
24. C. P. T. GROTH and J. J. GOTTLIEB. University of Toronto Institute for Aerospace Studies Report No. 327, October 1988.
25. J. J. GOTTLIEB, C. P. T. GROTH, F. LESAGE, and J. MAILLETTE. In Proceedings of the 11th International Symposium on Ballistics. Vol. I. Brussels, Belgium, 1989. Departments of Armament and Ballistics and Applied Chemistry, Royal Military Academy Brussels. 1989. pp. 445–455.
26. A. K. JAIN. ASCE J. 102, 674 (1976).
27. H. W. LIEPMANN and F. E. GODDARD. J. Aeronaut. Sci. 24, 784 (1957).
28. F. KREITH. Principles of heat transfer. International Textbook Co., Scranton, PA. 1967.
29. S. CHAPMAN and T. G. COWLING. The mathematical theory of non-uniform gases. Cambridge University Press, London. 1970.
30. S. SRINIVASAN, J. C. TANNEHILL, and K. J. WEILMUENSTER. NASA Reference Publication 1181, August 1987.
31. S. SRINIVASAN and J. C. TANNEHILL. NASA Contract. Rep. 178 411, December 1987.
32. P. A. GNOFFO, R. N. GUPTA, and J. L. SHINN. NASA Technical Paper 2867, February 1989.
33. M. G. DUNN and S. W. KANG. NASA Contract. Rep. 2232, April 1973.
34. R. C. MILLIKAN and D. R. WHITE. J. Chem. Phys. 39, 3209 (1963).
35. F. G. BLOTTNER, M. JOHNSON, and M. ELLIS. Sandia Laboratories Report No. SC-RR-70-754, 1971.
36. C. R. WILKE. J. Chem. Phys. 18, 517 (1950).
37. A. HARTEN. J. Comput. Phys. 49, 357 (1983).
38. A. HARTEN. SIAM J. Numer. Anal. 21, 1 (1984).
39. P. L. ROE. J. Comput. Phys. 43, 357 (1981).
40. P. L. ROE and J. PIKE. In Computing methods in applied science and engineering VI. Edited by R. Glowinski and J. L. Lions, North-Holland Publishing Co., Amsterdam, 1984. pp. 499–518.
41. P. L. ROE. ICASE Report No. 84-53, 1984.
42. S. F. DAVIS. ICASE Report No. 84-20, 1984.
43. H. C. YEE. J. Comput. Phys. 68, 151 (1987).
44. S. R. CHAKRAVARTHY and S. OSHER. AIAA Paper No. 85-0363, 1985.
45. S. R. CHAKRAVARTHY and S. OSHER. Lect. Appl. Math. 22, 57 (1985).
46. P. K. SWEBY. SIAM J. Numer. Anal. 21, 995 (1984).
47. P. GLAISTER. J. Comput. Phys. 74, 382 (1988).
48. M.-S. LIOU, B. VAN LEER, and J.-S. SHUEN. J. Comput. Phys. 87, 1 (1990).
49. P. D. LAX and B. WENDROFF. Commun. Pure Appl. Math. 13, 217 (1960).
50. R. F. WARMING and R. M. BEAM. AIAA J. 14, 1241 (1976).
51. E. M. MURMAN. AIAA J. 12, 626 (1974).
52. H. M. GLAZ, P. COLELLA, J. P. COLLINS, and R. E. FERGUSON. AIAA J. 26, 698 (1988).
53. M. BEN-ARTZI. J. Comput. Phys. 81, 70 (1989).
54. H. C. YEE and J. L. SHINN. AIAA J. 27, 299 (1989).
55. T. R. A. BUSSING and E. M. MURMAN. AIAA J. 26, 1070 (1988).
56. D. KAMOWITZ. ICASE Report No. 86-67, November 1988.